University of West Attica

School of Engineering

Department of Biomedical Engineering

Imaging tools in preclinical research micro CT, SPECT, PET

Irenaios Pilatis

Supervisor:
George Loudos, Assistant Professor University of West Attica

Athens, 2021

this page intentionally left blank

THESIS

Imaging tools in preclinical research micro CT, SPECT, PET

Irenaios Pilatis

EXAMINING COMMITTEE

George Loudos, Assistant Professor, University of West Attica

Georgios Lountos

Digitally signed by Georgios Lountos
Date: 2021.05.05 15:47:53 +03'00'

Dimitrios Glotsos, Associate Professor, University of West Attica

Dimitrios Gklotsos

Digitally signed by Dimitrios Gklotsos
Date: 2021.04.22 10:04:03 +03'00'

Stratos David, Assistant Professor, University of West Attica

Efstratios David

Digitally signed by Efstratios David
Date: 2021.04.21 13:46:59 +03'00'

ΔΗΛΩΣΗ ΣΥΓΓΡΑΦΕΑ ΔΙΠΛΩΜΑΤΙΚΗΣ ΕΡΓΑΣΙΑΣ

Ο κάτωθι υπογεγραμμένος Ειρηναίος Πηλάτης του Βασιλείου, με αριθμό μητρώου 11073 φοιτητής του Πανεπιστημίου Δυτικής Αττικής της Σχολής Μηχανικών του Τμήματος μηχανικών βιοϊατρικής, δηλώνω υπεύθυνα ότι:

«Είμαι συγγραφέας αυτής της πτυχιακής/διπλωματικής εργασίας και ότι κάθε βοήθεια την οποία είχα για την προετοιμασία της είναι πλήρως αναγνωρισμένη και αναφέρεται στην εργασία. Επίσης, οι όποιες πηγές από τις οποίες έκανα χρήση δεδομένων, ιδεών ή λέξεων, είτε ακριβώς είτε παραφρασμένες, αναφέρονται στο σύνολό τους, με πλήρη αναφορά στους συγγραφείς, τον εκδοτικό οίκο ή το περιοδικό, συμπεριλαμβανομένων και των πηγών που ενδεχομένως χρησιμοποιήθηκαν από το διαδίκτυο. Επίσης, βεβαιώνω ότι αυτή η εργασία έχει συγγραφεί από μένα αποκλειστικά και αποτελεί προϊόν πνευματικής ιδιοκτησίας τόσο δικής μου, όσο και του Ιδρύματος.

Παράβαση της ανωτέρω ακαδημαϊκής μου ευθύνης αποτελεί ουσιώδη λόγο για την ανάκληση του πτυχίου μου».

Ο Δηλών

Ειρηνάιος Πηλάτης

20 Απριλίου 2021

ABSTRACT

Over the past decades the area of medical imaging has evolved rapidly. This is demonstrated by the increasing number of imaging systems in hospitals and research facilities and the increasing number of people specializing in the field. New technologies have emerged to support ionizing radiation imaging techniques, based on one simple goal, which is making people life healthier and easier. Most of diagnostic protocols include the use of ionizing radiation, as the main source of signal production and detection. These techniques aim to be fast and minimally invasive, while providing lot of information about the health status of the subject, in terms of diagnostic characteristics.

In this project, the most common and popular imaging techniques will be discussed, which have been reviewed and analyzed. Namely, this study discusses the several X-ray procedures, such as the X-ray imaging and Computed Tomography. PET and SPECT are also part of this study and are presented in detail.

In the last part of this thesis, the results by a series of experiments are presented, executed to highlight their applicability, strong and weak points, as well as a wide range of applications that have been performed in a pre-clinical lab.

this page intentionally left blank

ΠΕΡΙΛΗΨΗ

Τις τελευταίες δεκαετίες, ο τομέας της ιατρικής απεικόνισης έχει εξελιχθεί ραγδαία. Αυτό αποδεικνύεται με τον αυξανόμενο αριθμό απεικονιστικών συστημάτων σε νοσοκομεία και ερευνητικά κέντρα και από την αύξηση του αριθμού των ατόμων, που εξειδικεύονται σε αυτόν τον τομέα. Οι νέες τεχνολογίες, που έχουν προκύψει, υποστηρίζουν τις τεχνικές απεικόνισης με τη χρήση ιονίζουσας ακτινοβολίας και έχουν ως στόχο να κάνουν τη ζωή των ανθρώπων ευκολότερη και υγιή. Τα περισσότερα διαγνωστικά πρωτόκολλα περιλαμβάνουν τη χρήση ιονίζουσας ακτινοβολίας, ως την κύρια πηγή παραγωγής και ανίχνευσης σήματος. Αυτές οι τεχνικές στοχεύουν να είναι γρήγορες και ελάχιστα επεμβατικές, παρέχοντας πληροφορίες σχετικά με την κατάσταση υγείας του ατόμου, όσον αφορά τα διαγνωστικά χαρακτηριστικά.

Σε αυτή την εργασία, θα συζητηθούν οι πιο κοινές και γνωστές τεχνικές απεικόνισης, οι οποίες έχουν αναθεωρηθεί και αναλυθεί. Συγκεκριμένα, αυτή η εργασία αναφέρεται σε διάφορες διαδικασίες, που χρησιμοποιούν ακτίνες Χ, όπως την απεικόνιση με ακτίνες Χ και την υπολογιστική τομογραφία. Επίσης, οι τεχνικές PET και SPECT αποτελούν μέρος αυτής της μελέτης και παρουσιάζονται λεπτομερώς.

Στο τελευταίο μέρος της εργασίας, παρουσιάζονται τα αποτελέσματα μιας σειράς πειραμάτων, τα οποία εκτελούνται, για να επισημάνουν τη δυνατότητα εφαρμογής τους, τα πλεονεκτήματα και μειονεκτήματά τους, καθώς και το ευρύ φάσμα εφαρμογών, που έχουν εκτελεστεί σε προκλινικό επίπεδο.

this page intentionally left blank

Contents

List of abbreviations

UV	UltraViolet
FID	Focus-to-Image Distance
OID	Object-to-Image Distance
CMOS	Complementary Metal Oxide Sensor
CsI	Cesium Iodide
CCD	Charged Couple Device
DQE	Detective Quantum Efficiency
E_B	Binding Energy
I_0	Incident X-ray Intensity
CT	Computed Tomography
EBCT	Electron Beam Computed Tomography
UPS	Uninterruptible Power Supply
MPR	Multiplanar Reconstruction
$CTDI_{vol}$	Volume Computed Tomography Dose Index
MDCT	Multiple Detector Computed Tomography
SNR	Signal-to-Noise Ratio
FOV	Field of View
FT	Fourier Transform
HU	Hounsfield Unit
STP	Standard Temperature and Pressure
CNR	Contrast-to-Noise Ratio
LCD	Low Contrast Detail
PEI	Photoelectric Interaction
AAL	Attenuation Level
SPECT	Single-Photon Emission Computed Tomography
PMT	Photomultiplier Tube
FWHM	Full-Width at Half-Maximum
PET	Positron Emission Tomography
ML-EM	maximum-likelihood expectation maximum

1. Chapter Radiography

1.1 Electromagnetic spectrum

X-rays are high-energy electromagnetic radiation, used to image the human bones or regions of different tissue density (e.g., lungs). They are produced by accelerating electrons, smashing into an atom like copper or gallium. X-rays are classified into soft X-rays and hard X-rays. Soft X-rays wavelength ranges from 1-10 nanometers, between ultraviolet (UV) light and gamma rays in the electromagnetic spectrum (Image 1). Hard X-rays wavelength ranges about 100 picometers [1].

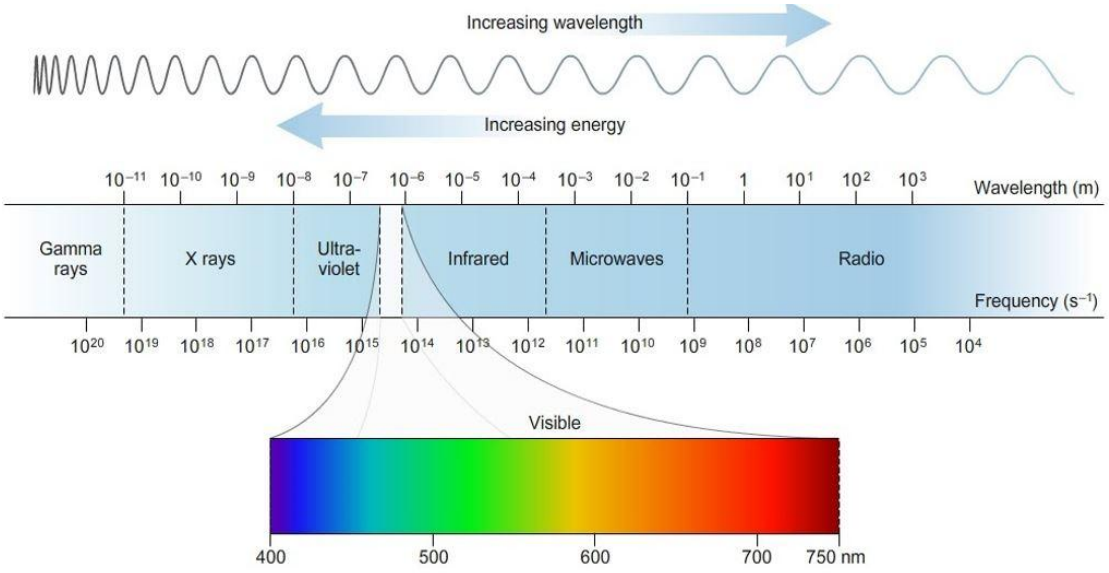

Image 1: Electromagnetic spectrum [2].

1.2 X-ray imaging geometry

The primary effect of radiography is to record an image of a 3D object (the patient) in 2D, resulting in superposition of the anatomy along each ray. This results to many effects that need to be considered, such as the design of equipment and the production of the images as well as their interpretation. In general, for each projection there will be a region of clinical interest, somewhere between the entrance and exit surface of the region to be imaged. Considerable experience is required for the radiographer to choose the

geometrical variables and image this region based on superficial visible or palpable landmarks. These variables include focus-to-image distance (FID), object-to-image distance (OID), projection direction (lateral, cranio-caudal) or angulation, central point and beam collimation area. In some cases, the correct projection of joint spaces needs also to be considered. The pixel intensity values of the radiography image represent the X-ray attenuation following up the superposition of individual attenuations (Image 2), due to different tissue composition, density and thickness, along each ray path [3].

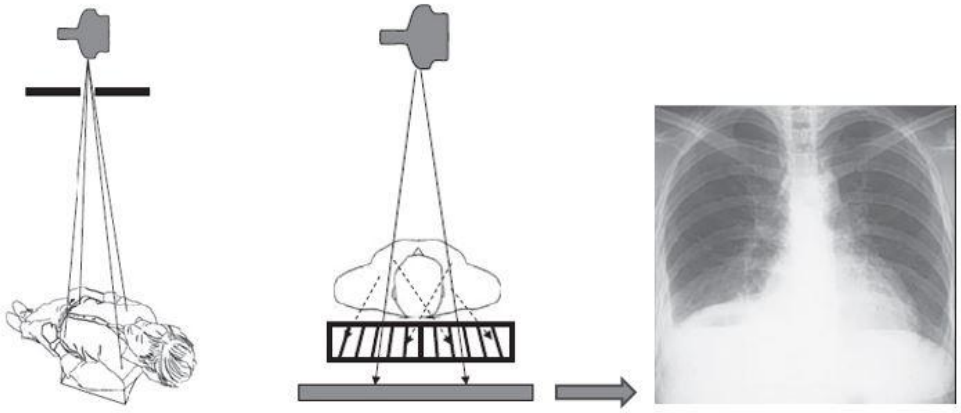

Image 2: 2D projection geometry of a 3D object produces a planar image (radiograph) [4].

1.3 X-ray tube components

The X-ray tube is consisted of cathode and anode (Image 3). Usually, there is a separate electrical circuit to lead the electrons out of the cathode in a natural way, so the electrons are attracted to the positively charged anode, using elements essential to promoting the phenomenon of thermal emission (e). Also, cathode has a high melting point (~ 3400 ^{o}C), a big and a small focal spot (Image 4).

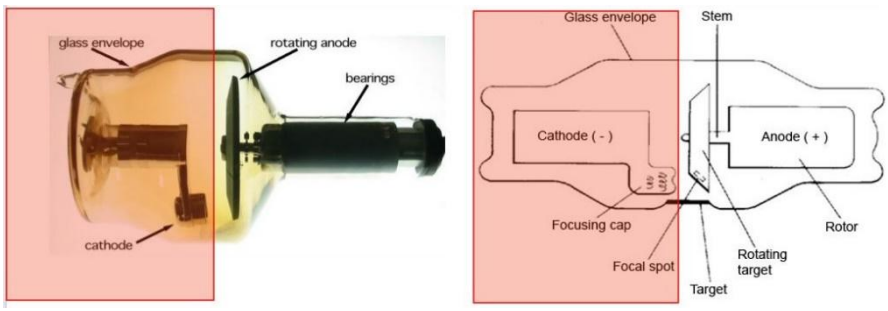

Image 3: X-ray tube components [5].

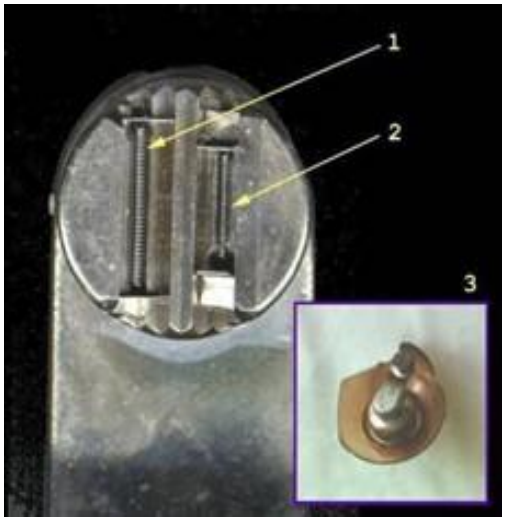

Image 4: Cathode, where 1: the big focal spot, +: low surface heat load intensity, -: low spatial resolution, increased ambiguity and 2: the small focal spot, which shows the opposite effects from the big focal spot [5].

On the other side, the anode is usually made of materials with the following conditions: they are metals with high melting point and a relatively high atomic number, thus a lot of electrons revolve around the core (Image 5) [5].

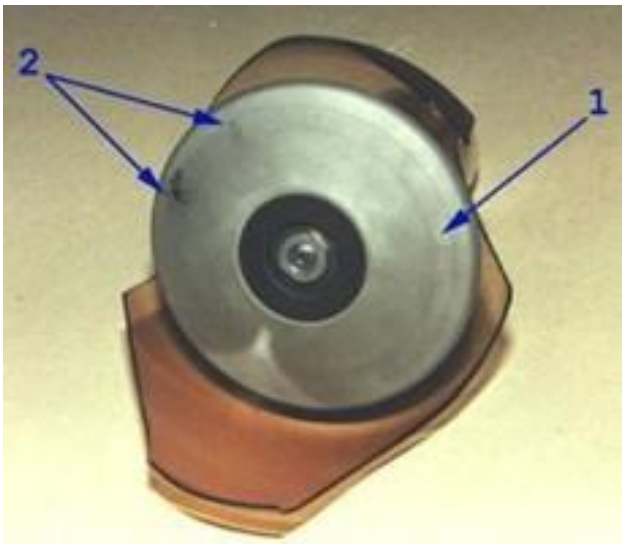

Image 5: Anode, 1: e^- orbital, 2: anode destruction [5].

1.4 Indirect detection

The indirect detection takes place by X-ray photon conversion to visible light photons. At the past, photographic films had been used as well as photo stimulating phosphors (Image 6) that were pioneered by Fuji in the 1980s. Nowadays, X-rays detectors are fluorescent materials that are usually coupled with complementary metal oxide sensor (CMOS) (Image 7). The cesium

iodide (CsI) is used to convert the X-ray photons to light, the photodiode transistor array converts the light to electrons, where each photodiode equals to one pixel. A great disadvantage of this type of detection is the diffraction of light [6, 7].

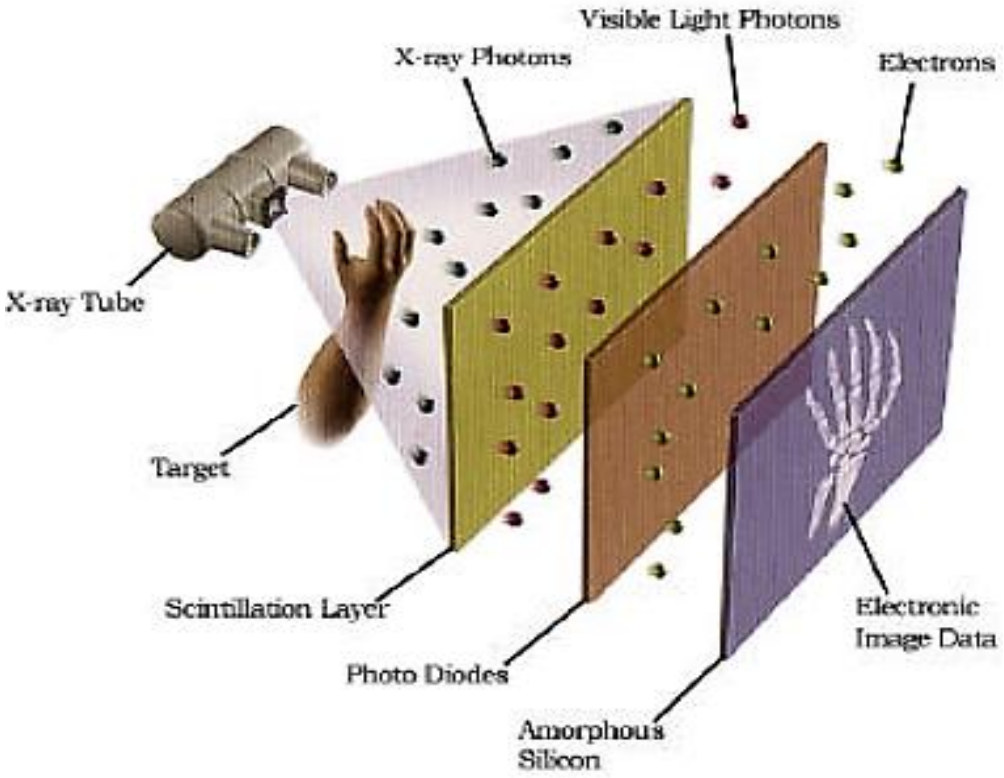

Image 6: Operating principles diagram of indirect detection [8].

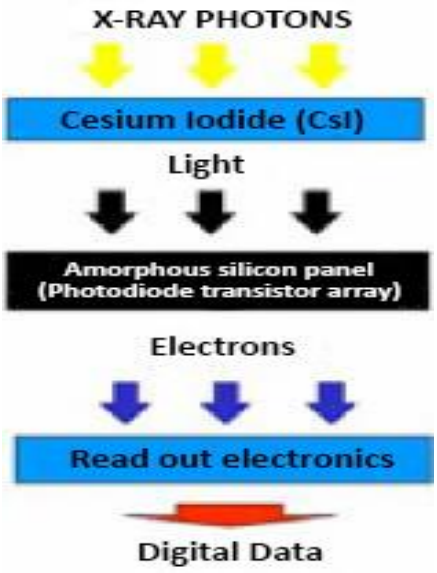

Image 7: Block diagram of indirect detection, using CMOS sensor [8].

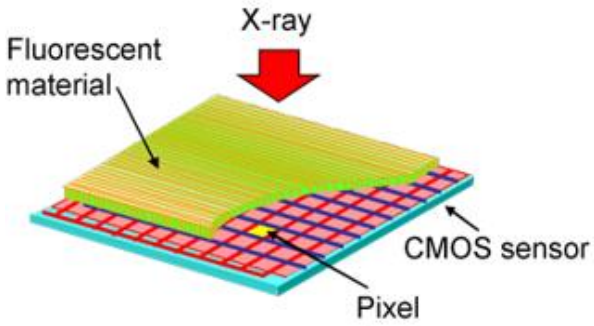

Image 8: A scheme of a CMOS sensor [8].

1.5 Direct detection

The direct detector instantly converts X-rays into an electronic signal, then capture images using CMOS or charged couple device (CCD) detectors. The light diffuses and disappears as it passes through the scintillator before it reaches the CCD or CMOS detector. In this type of detection, X-rays are not converted to light (Image 9), thus blurring is reduced significantly, and the images are sharper, with better contrast than those produced using indirect detection techniques. In addition, the high value of Detective Quantum Efficiency (DQE) enables high efficiency at lower dose of X-rays. The advantages of this type of detection are: the high value of DQE and the absence of light diffraction (Image 10) [9, 10] [11].

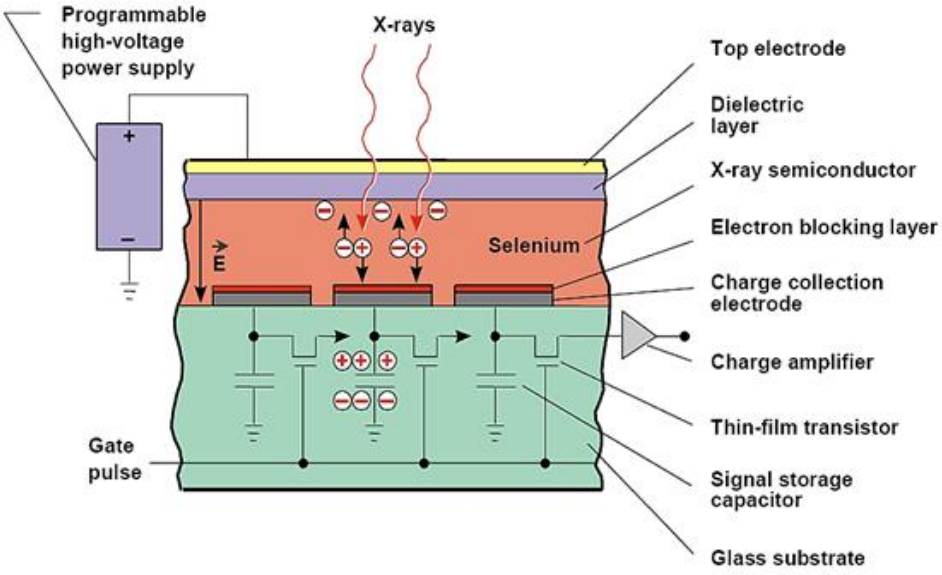

Image 9: A scheme of a direct detector [12].

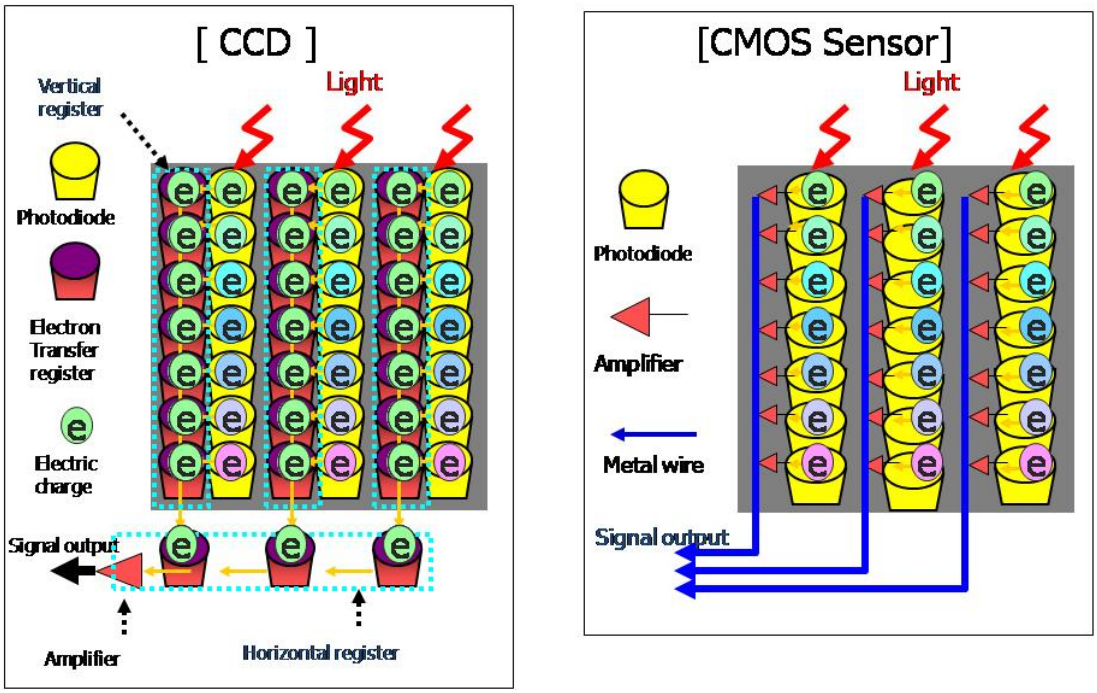

Image 10: Diagrams of a CCD (left) and a CMOS (right) sensor [12].

1.6 Anti-scatter collimator

Generally, the collimators are used to reduce the scattered radiation and they are placed between the patient and the cassette/detector. The anti-scatter diaphragm is flat, rigid, consisted of high X-ray absorption lead strips and allows X-ray passage to be parallel to the lead strips. The space between the lead strips is filled with a low absorption material. The primary radiation can effectively pass though the gaps without being absorbed from the lead strips (Image 11). The collimator uses the principles of geometry to reduce the number of scattering photons, which reaching the detector. The dimensions, that determine the efficiency of the anti-scatter diaphragm, are the thickness and the height of the lead strips and the thickness of the gap between them.

The grid ratio is a measure of the height of the lead strip to the interspace distance. The most common values of grid ratio are 8:1, 10:1 and 12:1. Also, the advantage of the anti-scatter collimator is that improves the contrast but the disadvantage is that increases the absorbed dose by the patient [13].

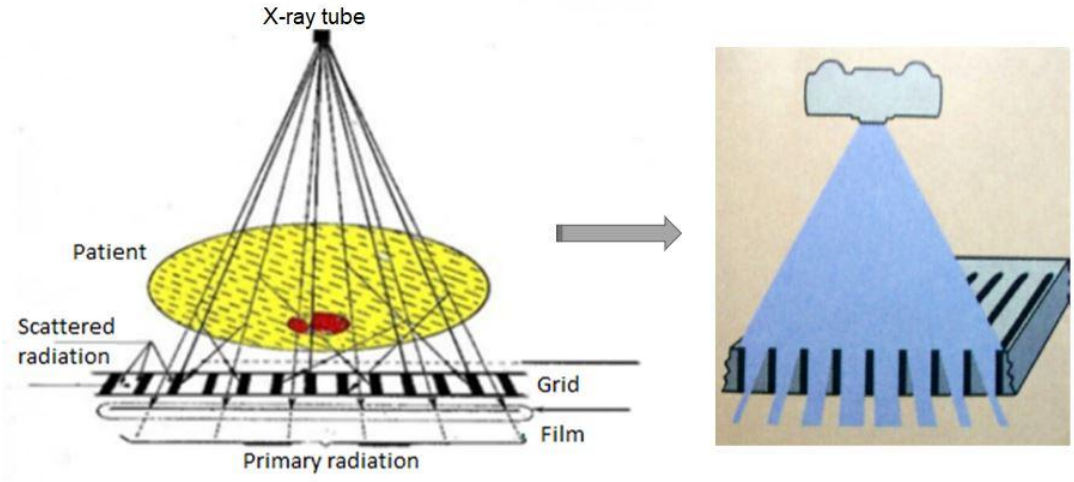

Image 11: Anti-scatter collimator [5].

1.7 Radiation matter interactions

The physics of events, that occur when photons and electrons interact with matter, are important for diagnostic radiology. In the photoelectric effect, the incident photon interacts with an atom and disappears. A photoelectron is ejected (Image 12). The photoelectric effect can only take place if the photon energy $h\nu > E_B$ (binding energy). The most probable electron shell to lose an electron is the one that satisfies this constraint and has the highest binding energy.

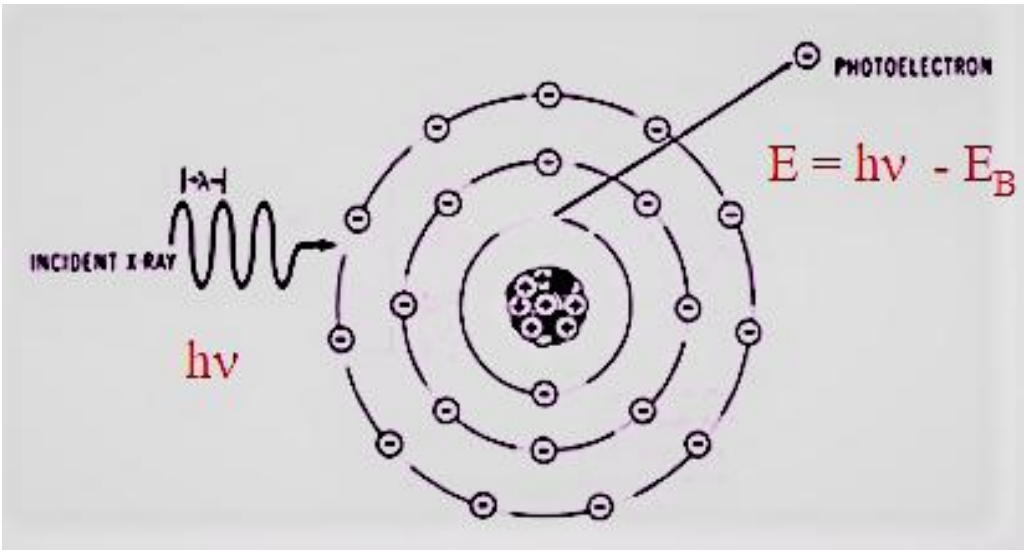

Image 12: The photoelectric effect [5].

Compton scattering is the interaction between electromagnetic radiation and an outer layer electron, but in this case, there is an energy transfer to the

electron (Image 13). The energy range is such that relativity and quantum mechanics must be used to derive expressions for the cross section. Both the photon and the electron must be considered as particles.

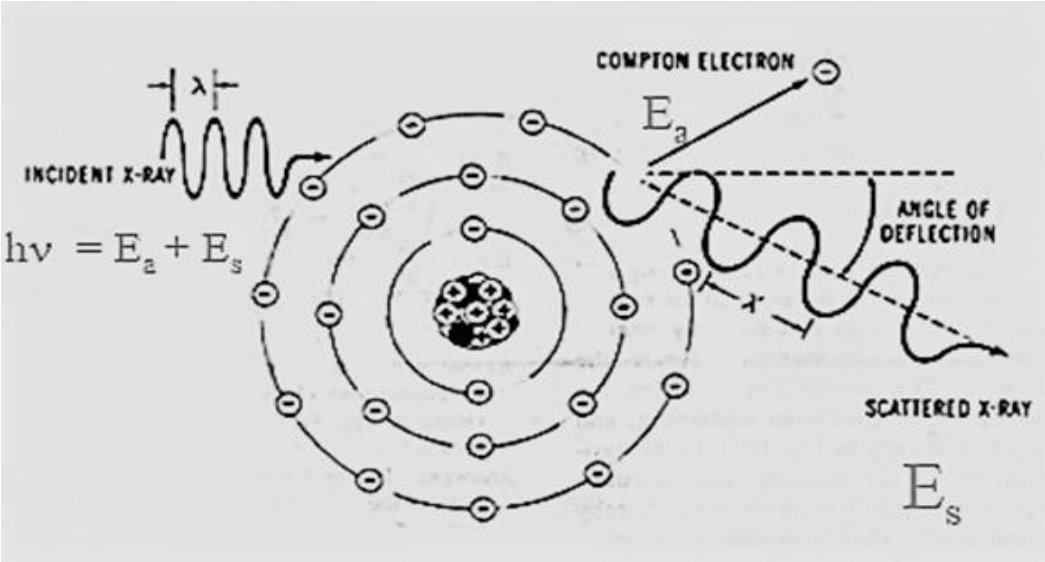

Image 13: The Compton effect [5].

When a high energy photon passes near to an atomic nucleus, the photon may interact with the nuclear Coulomb field by a process called pair production. The photon is converted into an electron-positron pair, each with its own kinetic energy (Image 14). Pair production cannot take place for photons with energies less than the energy threshold (1022 keV). As pair production occurs in the field of the nucleus, the cross section for this interaction varies approximately as Z^2, where Z is the nuclear charge.

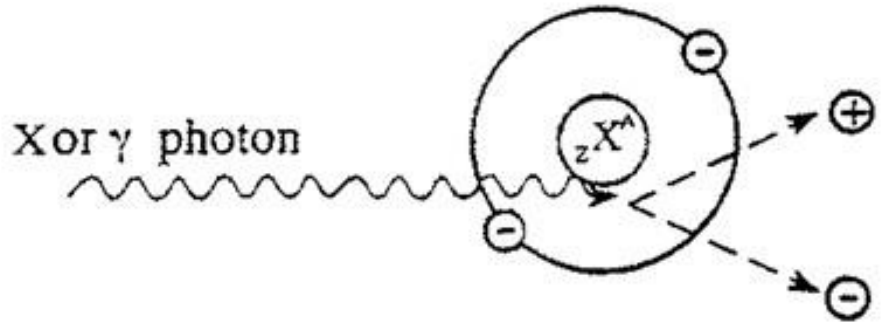

Image 14: The Pair production [5].

The most important effects at the radio-diagnostic field are the photoelectric and Compton effect. The photoelectric effect does not produce X-radiation (photon removal-X from the incident beam) and the Compton effect is

accompanied by scattered X-radiation, but it is undesirable for image production due to incorrect information about location. The differences in primary radiation, photoelectric and Compton interaction effects is the signal recorded by the image detectors in Radiology and these interactions occur at atomic level but are recorded macroscopically [5].

1.8 X-ray attenuation

Photons may undergo more than one interaction as they pass through bulk material, so an initial scatter interaction might be followed by a second scattering process which in turn might be followed by a third scatter, photoelectric absorption or no further interactions with the photon leaving the bulk material. To consider this macroscopic behavior of primary photons traversing matter linear attenuation and mass attenuation coefficients are used (Image 15), which are simply related to the total cross section. The exit beam from the bulk material will also comprise both primary and scattered photons. Such effects are best estimated using Monte Carlo techniques.

Considering a thin uniform slab of material of thickness dx, which is irradiated with a beam of photons incident normally on the slab. Individual photons may pass through the slab without interacting or they may be absorbed or scattered. The differential intensity (dI) is given by (eq. 1):

$$dI = -\mu I dx \rightarrow \int_{I_o}^{I} \frac{dI}{I} = -\mu \int_{0}^{T} dt \rightarrow \ln \frac{I}{I_o} = -\mu T \rightarrow I = I_o e^{-\mu T} \quad (1)$$

where I_0 = incident X-ray intensity and T = total object thickness in the direction of propagation of the X-rays.

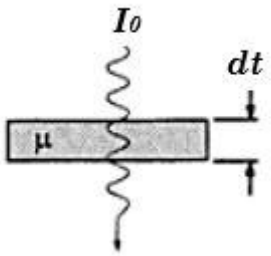

Image 15: Schematic illustration of linear attenuation [5].

The linear attenuation coefficient μ expresses the probability of attenuation of an X-ray photon per unit thickness of a material (dimensions of inverse length $\frac{1}{[l]}$). Also, μ is a function of the X-ray beam energy, the atomic number of the material and electron density of the material, i.e. μ (Z, ρ_e, E). Dividing μ, material density ρ provides the mass attenuation coefficient (dimensions $\frac{[l^2]}{[m]}$). X-ray photons interactions with matter at the atomic level are responsible for the resulting macroscopic attenuation of the incident (primary) beam of uniform intensity. Both μ and μ/ρ express the total attenuation, due to all interactions. In the diagnostic X-ray range (10-150 keV) the major participating interactions are the photoelectric effect and Compton scatter (Image 16) [14, 15].

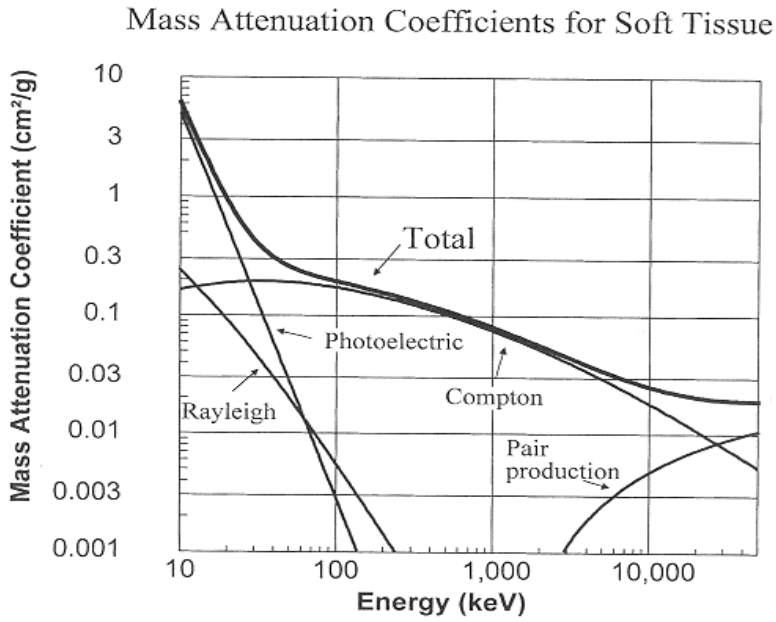

Image 16: Diagram of mass attenuation coefficient (cm^2/g) versus energy (keV) [5].

1.9 Typical X-ray spectrum of a CT scanner

The X-ray spectra used in Computed Tomography (CT) imaging are some of the most difficult spectra used in medical radiological X-ray imaging, generally because of the typically higher tube potentials used and the greater amount of added filtration for the central ray (Image 17). Usually, high X-ray energies are used in CT. The efficient energies (equivalent monoenergetic beam energies) of the 80 and 140 kVp spectra are 40 and 60 keV respectively [16].

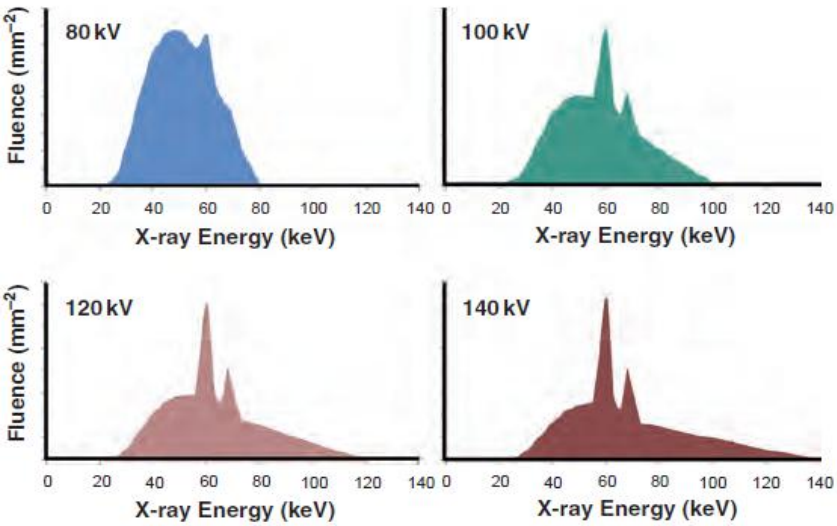

Image 17: Diagram of fluence (mm^{-2}) versus X-ray energy (keV) [5].

1.10 Basic parameters that affect X-ray imaging

High voltage affects the maximum energy of the continuous E_{max} spectrum, resulting in a change in its energy content (quality). The number of photons (intensity-quantity) of the beam is proportional to kVp (2 curve area), if the high voltage (kVp) is less than the characteristic threshold (50 kVp). If it is above this value, then the attributes always appear in the same position (100 kVp) (image 18).

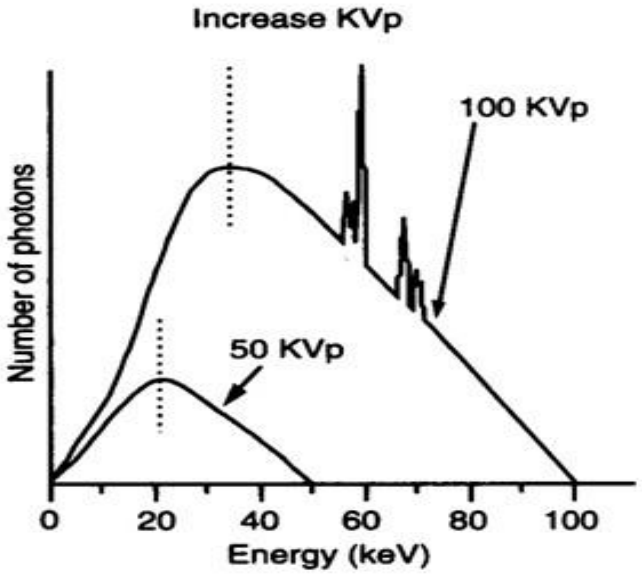

Image 18: Diagram of the number of photons versus energy (keV [5]).

The number of photons produced during the irradiation is directly proportional to the current of the lamp (mA) (e^- number accelerated by the cathode to the anode directly proportional to irradiation time (ms to mins) irradiation analogue of their product (mAs). The maximum energy as well as the shape of the energy spectrum, does not change. The characteristic radiation is independent of the intensity of the lamp current (Image 19), but its intensity changes (Image 20) [5].

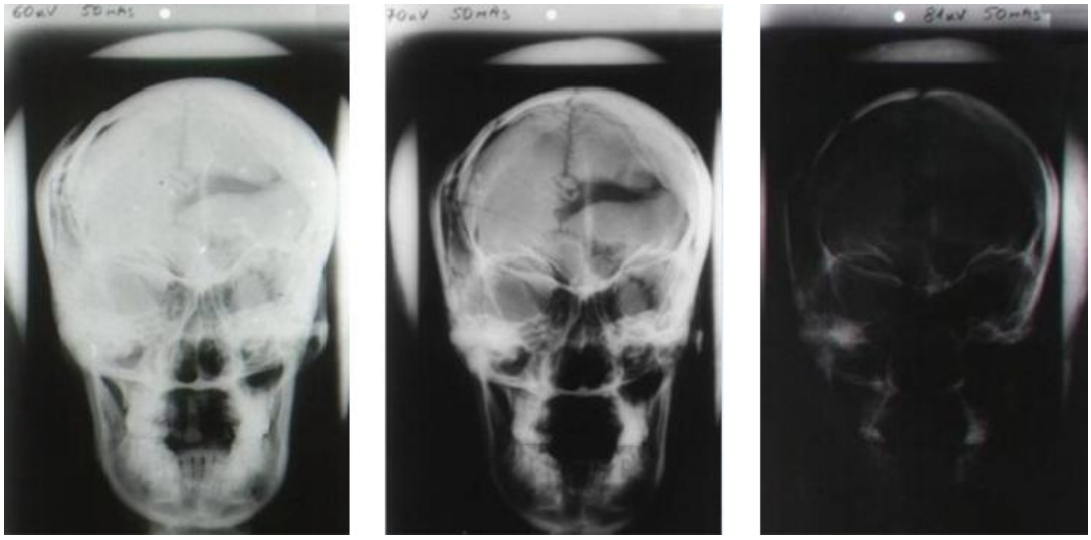

Image 19: From left to right: 60 kVp-50 mAs, 70 kVp-50 mAs, 81 kVp-50 mAs [5].

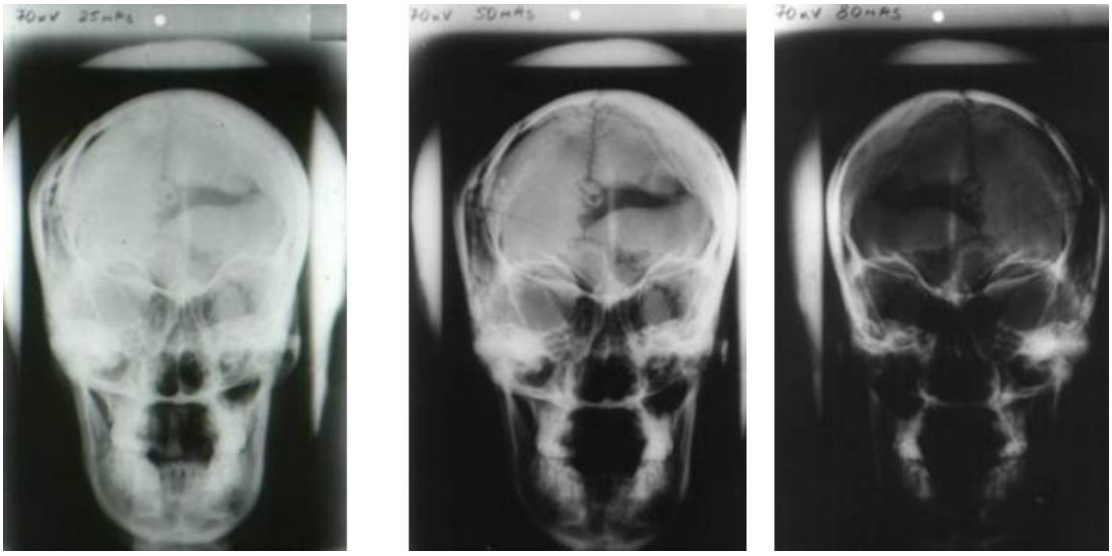

Image 20: From left to right: 70 kV-25 mAs, 70kV-50 mAs, 70 kV-80 mAs [5].

1.11 X-ray reason of use

The advantages of X-ray usage are that they can be used to easily diagnose conditions, such as tumors, without surgery and they produce images with

medium quality. On the other hand, the X-rays are dangerous, mutate cells, causing ionization and leading to cancer, also the bones absorb the radiation. But for imaging purposes, dose is reasonably low. To conclude, X-rays are not one hundred percent safe, however they are useful and can be controlled and used in the safest way possible [17].

this page intentionally left blank

2. Chapter Computed Tomography (CT)

2.1 How does a CT works?

Unlike a conventional X-ray, which uses a stationary X-ray tube, a CT scanner uses a motorized X-ray source that rotates around the circular opening (or as usually called the center of the circle, the isocenter) of a donut-shaped structure called a gantry. During a CT scan, the patient lies on a bed that slowly moves through the gantry while the X-ray tube rotates around the patient, shooting narrow beams of X-rays through the body. CT scanners use special digital X-ray detectors, which are located directly opposite the X-ray source. As the X-rays leave the patient, they are picked up by the detectors and transmitted to a computer (Image 21).

Each time the X-ray source completes one full rotation, the CT computer uses sophisticated mathematical techniques to construct several 2D image slices of the patient. The thickness of the tissue represented in each image slice can vary depending on the CT machine used, but usually ranges from 1-10 millimeters. The X-ray scanning process is then repeated to produce more image slices. This process continues until the desired number of slices is collected [18, 19].

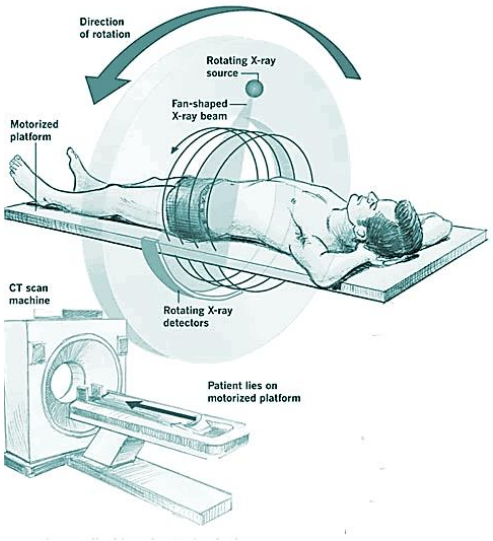

Image 21: Schematic illustration of a CT scanner system [20].

2.2 CT generations

The CT generations are identified primarily on the basis of the geometry of the mechanical scanning motions. Each successive generation has shown improvement in scanning mode, detection system and rotational movement (degrees of rotation) (Image 22). The main result of the changes made to each of the successive generations of CT systems has been an increase in scanning speed. Scan times have been reduced from approximately five minutes for early slice by slice acquisition units to less than 0.4 s for the current fourth-generation volume data acquisition (spiral or helical CT) scanners. The unique design of the electron beam CT (EBCT) systems, sometimes referred to as fifth-generation CT (Image 23), has made possible scanning times of 50 to 100 ms [21].

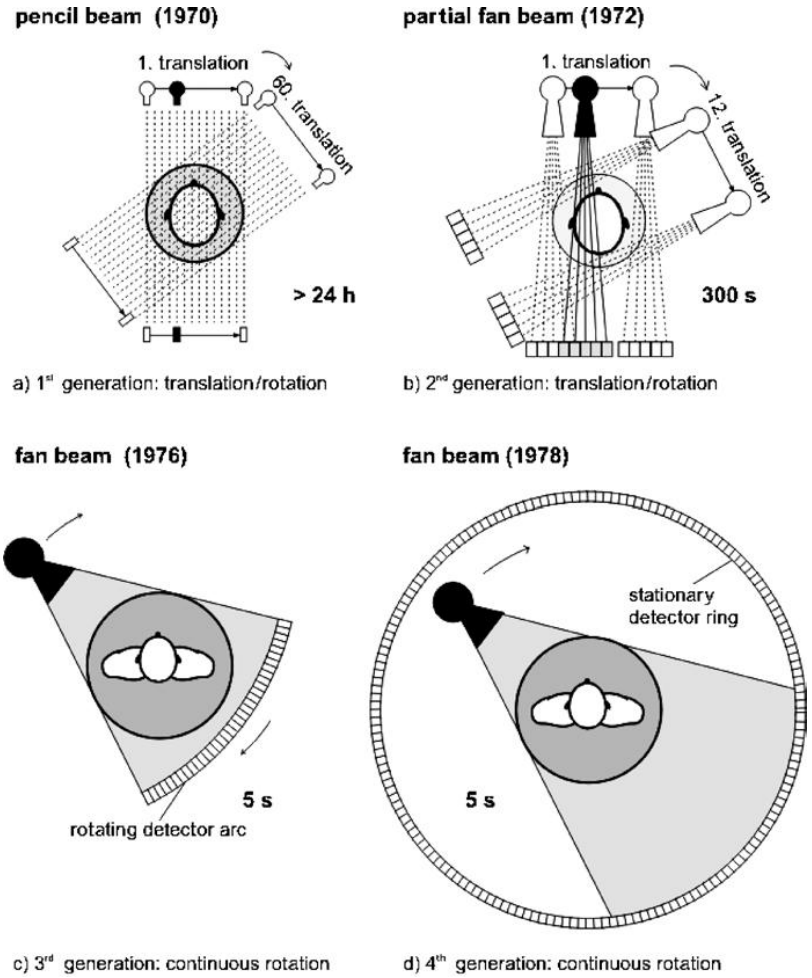

Image 22: Schematic illustration of CT generations [20].

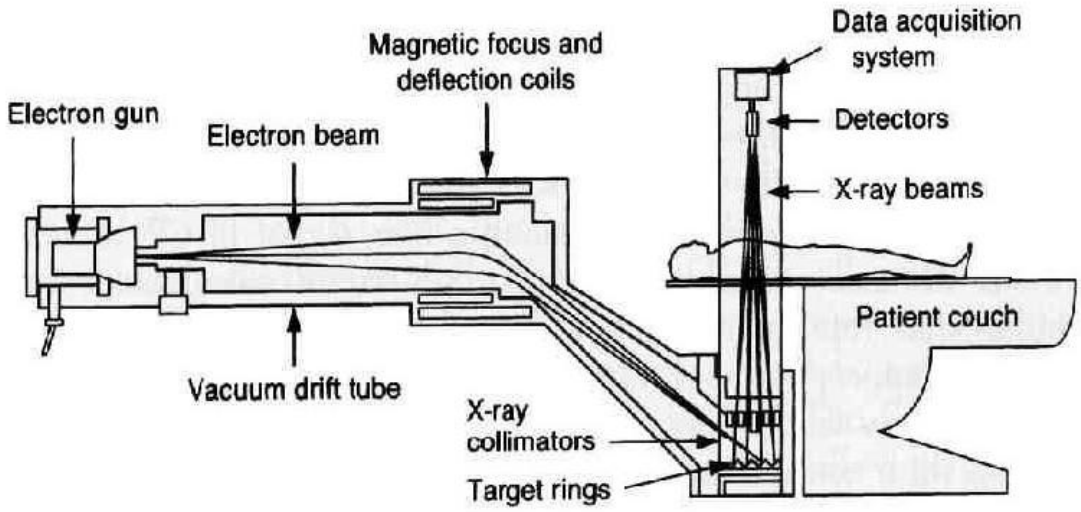

Image 23: Diagram of fifth-CT generation [22].

2.3 Single slice vs multi slice

The single slice CT scanner has an X-ray source and a single detector. The data acquisition involves the moving both tube and detector across the scanning plane to acquire a series of transmission measurements and all data are collected through a 180^{o} rotation. It is consisted of a gantry, where there is a X-ray tube, a high voltage generator, a detector, a pre-patient collimator and a post patient collimator, a table, a UPS and a control panel. The disadvantages of the single slice CT scanner are: the high patient dose, slow performance, low accuracy of MPR, low image quality and the artifacts.

The multi slice CT scanner is special because multiple detectors are placed next to each other so the CT can collect multiple slice data the same time (single scan). The multi slice can work on sequential and spiral mode. In the simplest multi slice CT there are rows of detectors. In these, the radiographer can set the slice thickness with the help of the collimator just as the conventional CT. An important thing is that usually the number of measurable slices is different from the number of detectors. The parts of this type of CT scan are: the gantry with the X-ray tube, the high voltage generator, the lesser light, the cooling system, the rows of detectors, the variable collimator and the control panel. The advantages are that performs special contrast study (biphasic, CT angiograms), limits the radiation doses, improves the spatial resolution, reduces the motion artifact, less contrast medium required,

changes the field area and produces 3D image (Image 24). On the other side, it is an expensive system and delivers high dose of radiation [18].

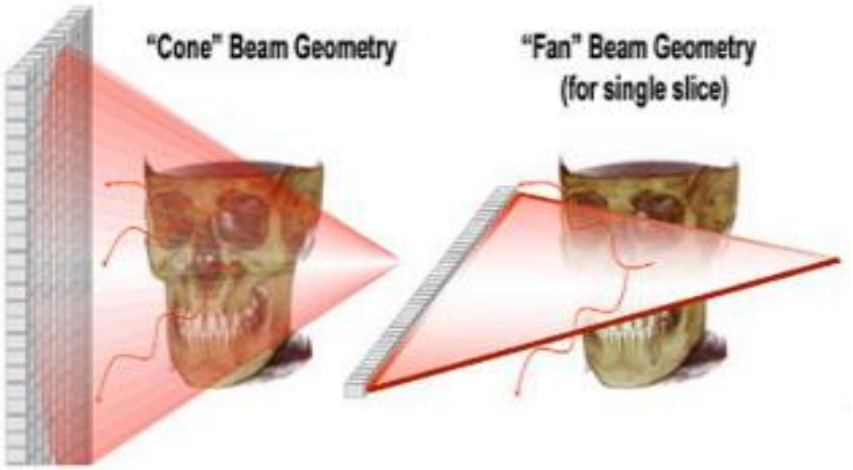

Image 24: Single slice CT versus multiple slice CT [22].

2.4 Single detector vs multiple detector

Older systems had only one detector line producing only one slice per acquisition. The multiple slice systems utilize detectors with multiple lines allowing a wider section of the patient to be imaged in the same acquisition period. In single detector CT slice thickness is manipulated by the collimator. In multiple detector CT slice thickness is disassociated from the X-ray beam width. The detector array width d (d = detector size as projected to the isocenter) determines the minimum slice thickness and the collimator determines the beam thickness (n x d) (Image 25). Cone beam CT is a multiple detector CT with very large number of detector arrays (typically 512x64 or 128 up to 320) [23-25].

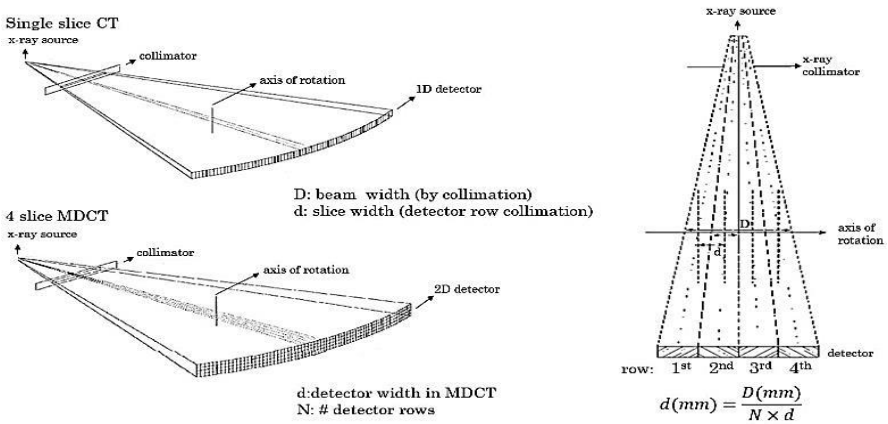

Image 25: Single detector CT versus multiple detector CT [22].

2.5 Sampling – Beam aperture

Assuming a block shaped beam with aperture Δs, then the required sampling interval Δr and the minimum number of detector samples can be calculated (Image 26). The convolution, o strongly reduces frequency content of the signal a, evident from f. Discrete sampling by the detector modelled by g yields the samples signal i. Sampling in the frequency domain (Image 26) corresponds to convolving f with the reciprocal pulse train h, resulting in the signal spectrum j corresponds to limit aliasing of f in j the contributions of f must be separated at least far enough. Assuming Δs = d in c then the main lobe width of d and f is 2 x 1/Δs. This means that the distance in pulses in f, which is 1/Δr must be at least equal to 2/Δs [26].

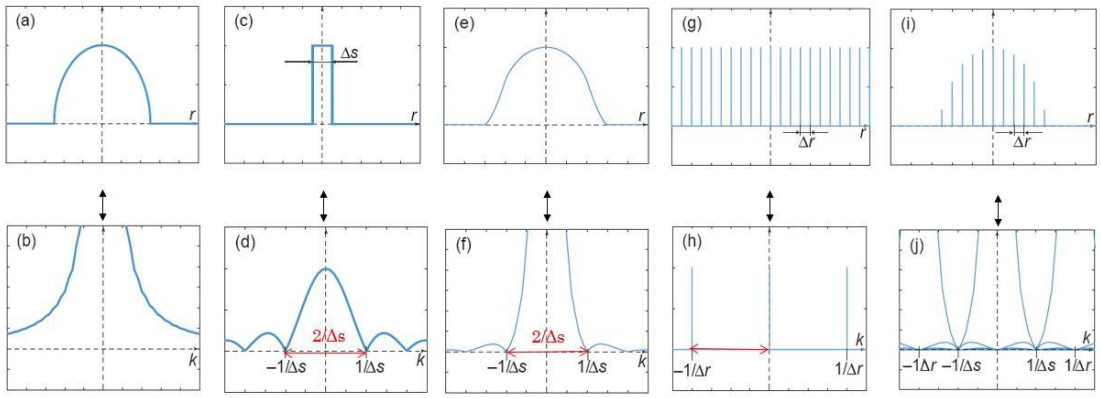

Image 26: Diagrams of r sampling (Δr) – beam aperture (Δs) [27].

2.6 Scanning

There are two methods of scanning: the sequential and the spiral. In the sequential method, a sequence of complete gantry rotation followed by table movement with the patient.

In the spiral method, there is a continuous gantry rotation and table movement (Image 27). The volume of raw data is generated from which axial images are reconstructed using interpolation. Also, the slip ring technology allowed transmissions of energy to rotating gantry without the need of cables.

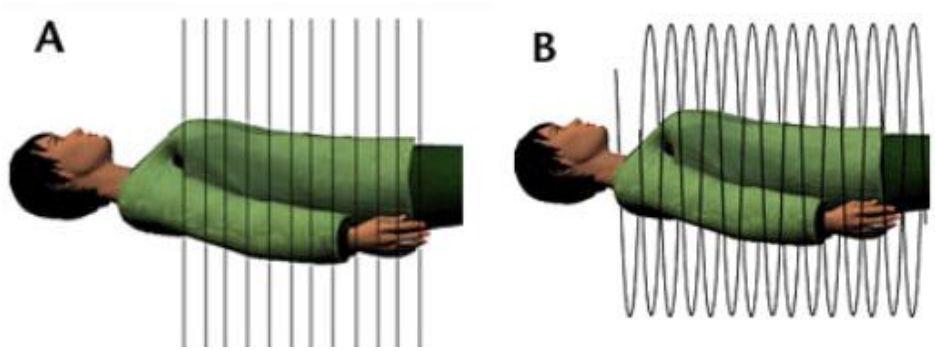

Image 27: Illustration of a) sequential and b) spiral method [27].

The most common slip-ring assemblies the use of metal rings or traces on one subcomponent (Image 28). Then, these interface with graphite or wire brushes that ride the rings' surfaces. So as that metal ring spins, transmissions conduct via the ring to the brush or vice versa [28].

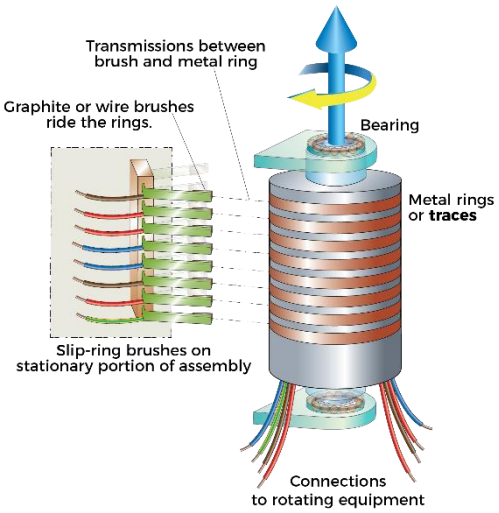

Image 28: Illustration of the slip – ring [27].

2.7 Spiral scan

Describing the spiral scan, the use of pitch will be introduced. The pitch is the distance (mm) that the patient table feed moves during a full X-ray light rotation through the section thickness (mm). Increasing the pitch with increase in speed, the absorption dose and examination time are reduced. On the other hand, the image resolution is worse. Users should monitor other parameters when changing pitch (Image 29). Th scanner may or may not automatically compensate for changes in pitch to maintain the planned

$CTDI_{vol}$. $CTDI_{vol}$ may not change in the expected manner if the scanner automatically adjusts other parameters when the pitch is changed. The relationship between $CTDI_{vol}$ and pitch for the different vendors are described below: $CTDI_{vol}$ inversely proportional to change in pitch, $CTDI_{vol}$ constant when the pitch is changed due to changes to other parameters GE, the relationship between $CTDI_{vol}$ and pitch depends on scan mode or Software version. If the value of pitch is 1, the coils of the helix are in contact and X-ray beams are contiguous for adjacent rotations. If the value of pitch < 1, then the coils of the helix overlap and the X-ray beams are not contiguous for adjacent rotations, i.e. there are gaps in between the X-ray beams and tissue is not irradiated. If the value of pitch > 1, the coils of the helix are separated and there is X-ray beam overlap, i.e. a volume of tissue is irradiated more than once per scan. Thus, a pitch value > 1 results in decreased patient dose but also decreased image quality (through fewer projections obtained, resulting in lower SNR). A pitch value of < 1 results in better image quality [29].

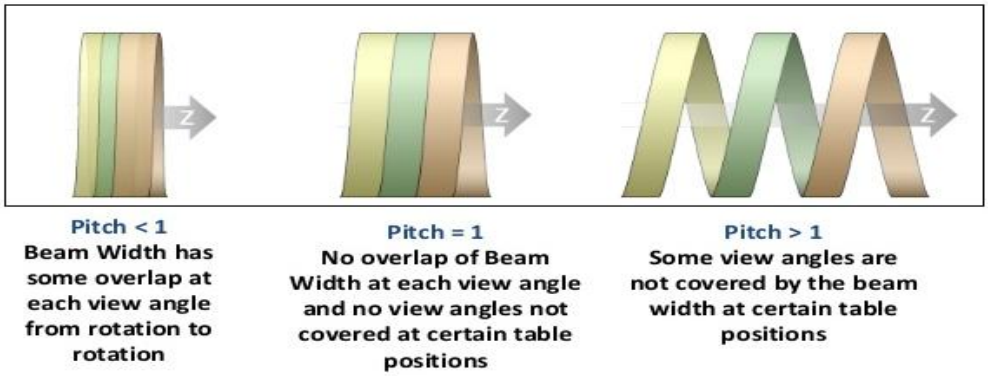

Image 29: Illustration of different values of pitch [29].

2.8 Concepts of helical scan and resolution

Each point in the helix represents a set of fan beam projection measurement. MD helical CT generates multiple sets of projection measurements at each rotation angle. The rotation angle is β along the z-axis, where z-axis is the location of the fan beam on the z-axis. Also, MDCT generates multiple helical sinograms. Helical z sampling pattern is a single slice helical scan (Image 30), exploiting 180^{o} projection measurements periodicity. Z-axis resolution is s and s/2 respectively.

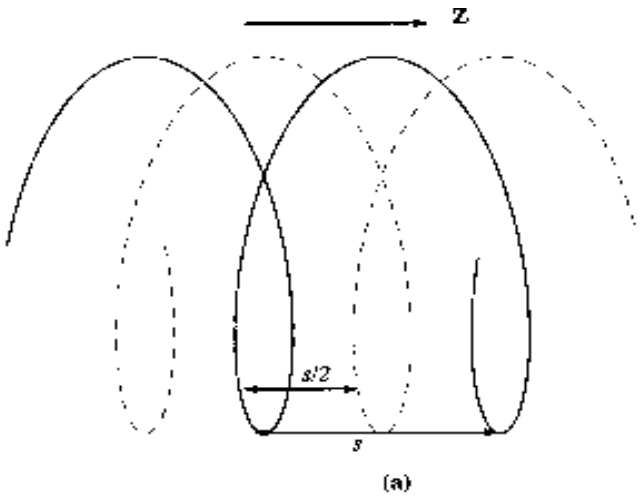

Image 30: Illustration of single slice helical scan [5].

Also, there is the helical z sampling pattern, where 4-slice helical MDCT, esxploiting 180^{o} projection measurements periodicity and z-axis resolution is d(s/4) and s/2 (s/8) (Image 31) [30].

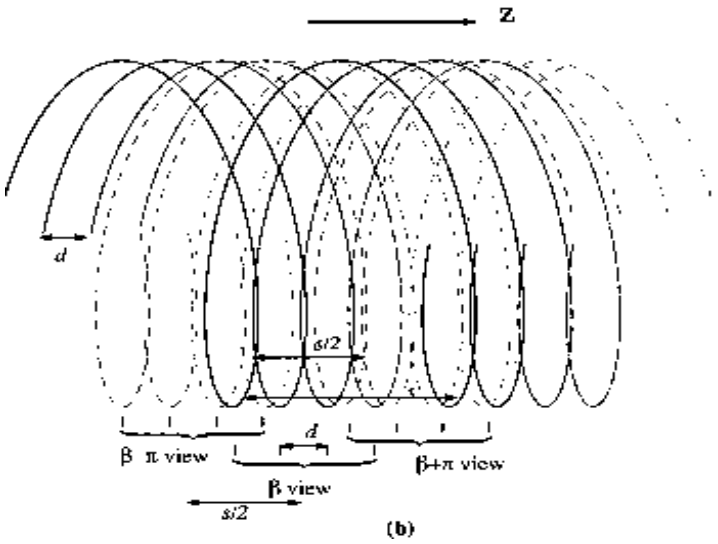

Image 31: Illustration of multiple slice helical scan [5].

2.9 Slice thickness and image noise

Although MDCT scanners enable a large number of thin slices to be reconstructed, the trade of between patient dose and image quality, in terms image noise and z-axis resolution, limits use of this capability (Image 32) [20].

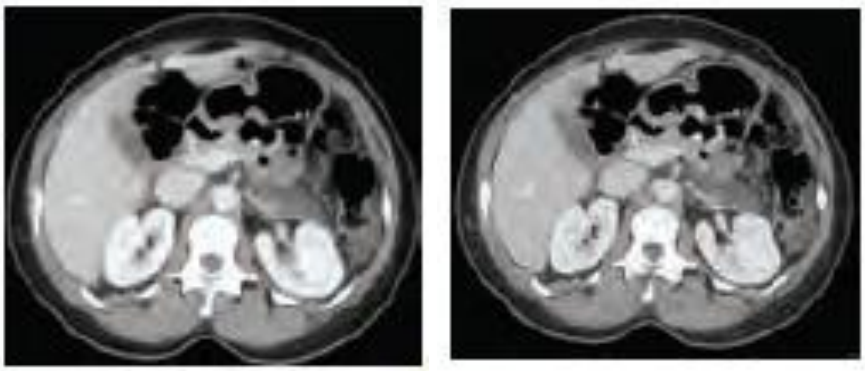

Image 32: Illustration of 40x5 mm slices (left) and 320x0.625 mm slices (right) [5].

2.10 Beam shaping filter

As most body regions have circular transversal in a CT slice, the X-ray fluence to the detector is high at the edges and low in the center. A beam shaping filter (bow tie filter) (Image 33) is used to attenuate more towards the perimeter of the FOV and less at the center to equalize the signal levels to the detector (Image 34) [31].

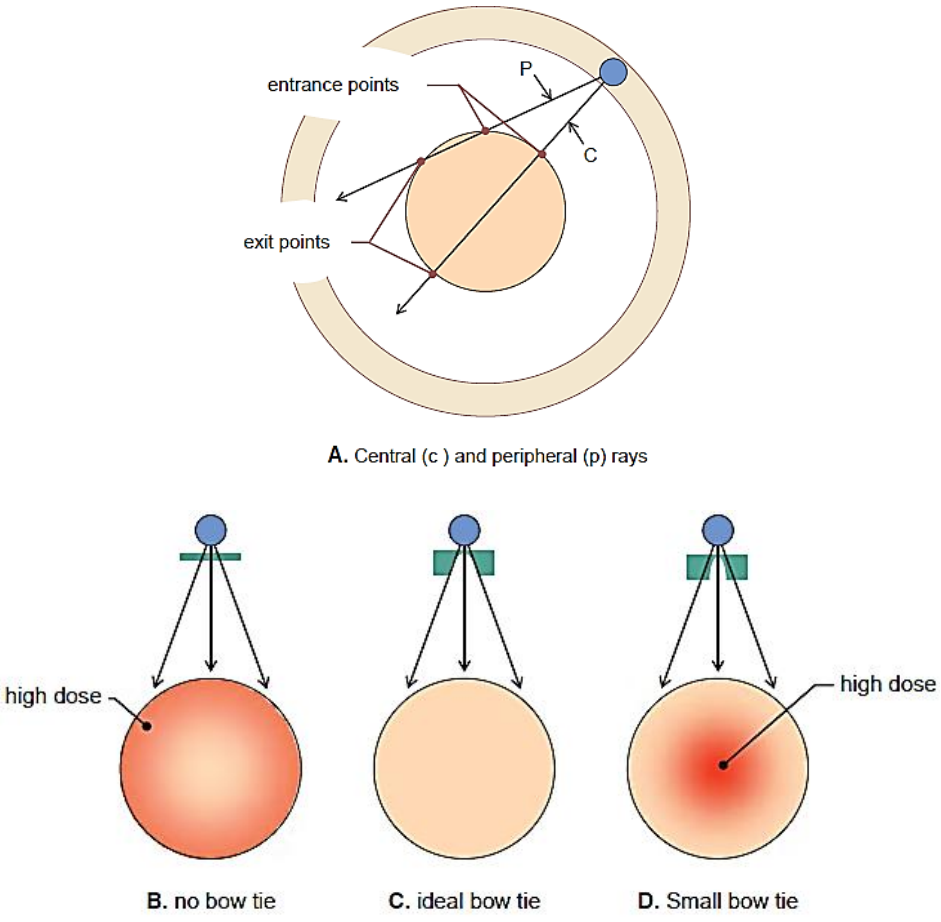

Image 33: Illustration of photon flow correction [31].

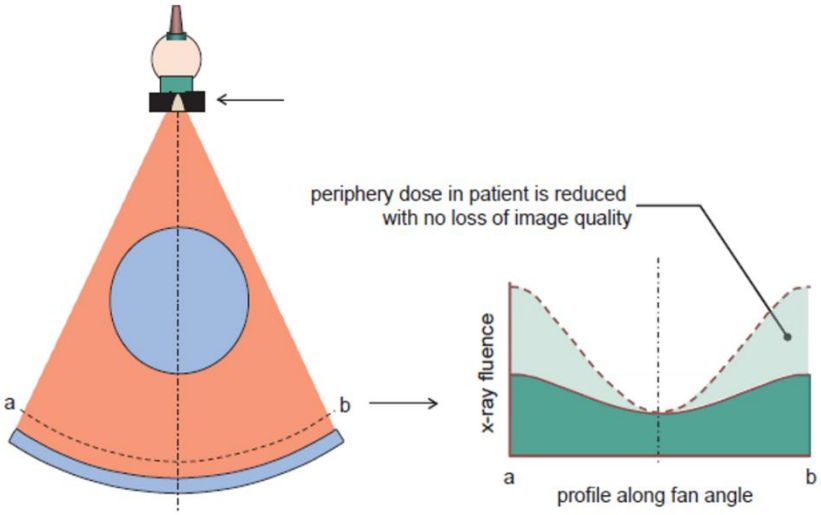

Image 34: The effect of the beam shaping filter is shown for a profile along the fan angle [31].

2.11 CT image reconstruction

The transversal viewing process results in a large one number of one-dimensional projective data corresponding to detector recordings for various projection acquisitions (0^o-360^o). The next goal is to calculate the two-dimensional function, which corresponds to the sagittal attenuation coefficients, i.e. of the tomographic image. The section consists distinct volume elements (volume elements, voxels) (Image 35). The in-plane resolution is the spatial resolution at x,y level, the pixel size is (Δx, Δy) and the z-axis resolution is the slice thickness [32, 33].

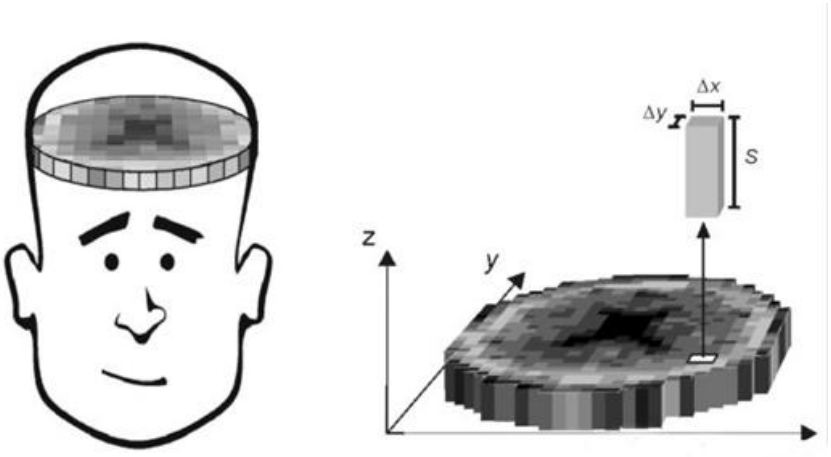

Image 35: CT image reconstruction [32, 33].

2.12 Projection data

The data (I_j, j = 1, …, N) recorded by one row of detector elements for a specific rotation angle θ, sample linear attenuation coefficient values (μ_i, i = 1, …, N) along a specific ray path j of the axial slice(Image 36). Ijs are corrected by the reading of a reference detector (I_r), outside the patient FOV, which records the primary beam intensity I_0 (eq 2). While, the X-ray attenuation is exponential logarithmic conversion of the measurements, allows the assumption that every measurement I_j corresponds to linear attenuation coefficient averages (eq. 3).

$$I_i = I_0 e^{-(\mu_1 d_1 + \mu_2 d_2 + \mu_3 d_3 + ... + \mu_N d_N)} \quad (2)$$

$$P_i = \ln\{\frac{I_0}{I_i}\} = \sum_{j=1}^{N} \mu_i d_i \quad (3)$$

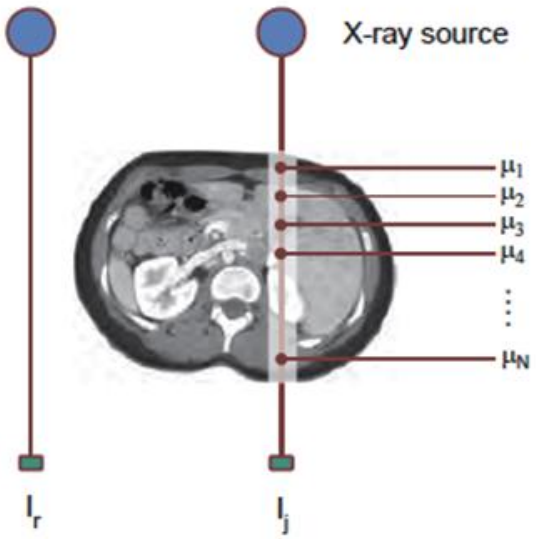

Image 36: Projection data [32, 33].

2.13 Back projection reconstruction

By the projection method, the radiation attenuation is known but we cannot know exactly where the attenuation occurred along the axis of interaction, that is along 35 cm in our example. To find out how many and exactly the photons absorbed, we apply the back projection method (Image 37).

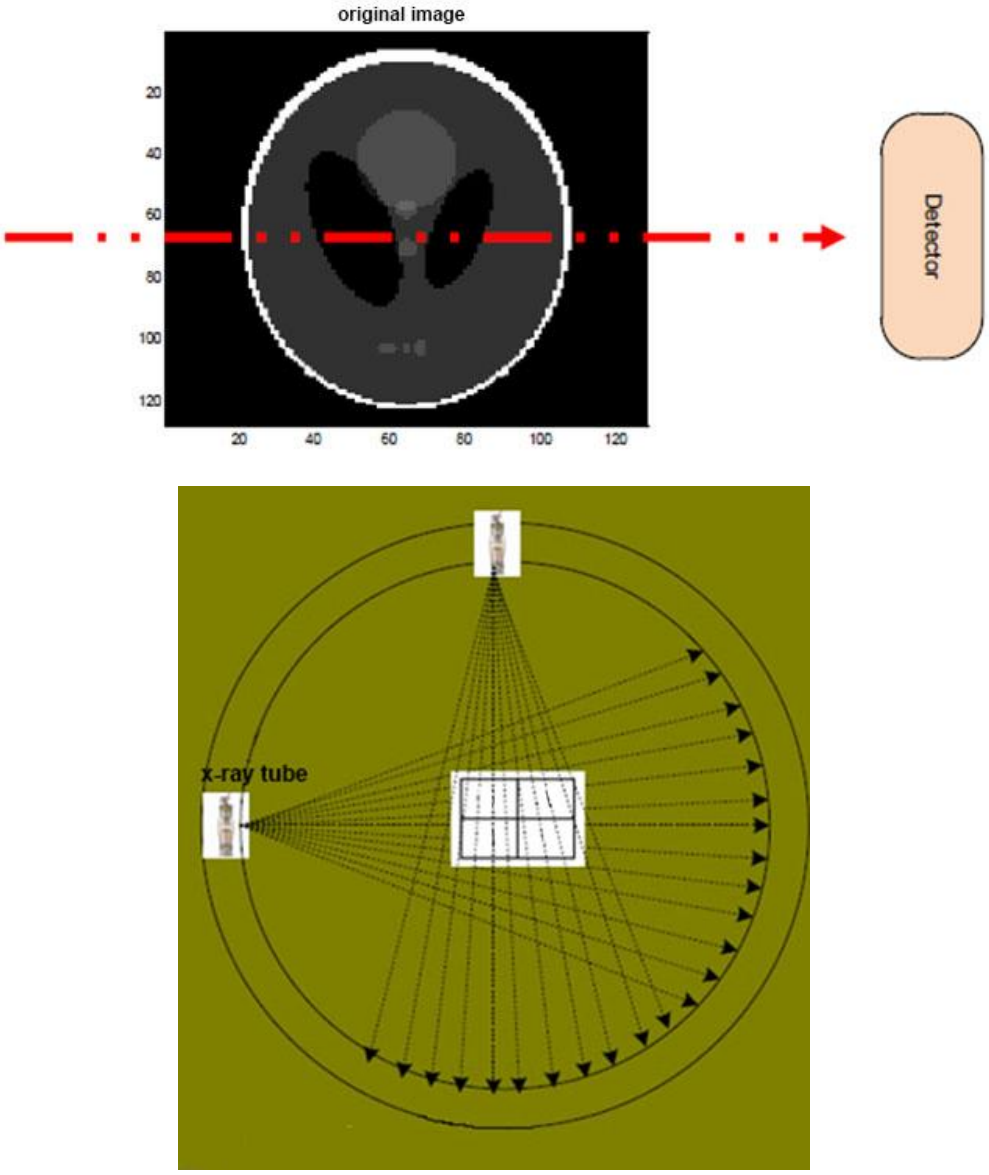

Image 37: Back projection reconstruction [34].

Back projection of a homogeneous circular object from 8 projections with 45^{o} step (Image 38). Dark gray tones correspond to a high display signal. The back projection as sum of projection images, resulting in a “pseudo star like image”, because of a small number of projections. With no standing the fact that the pseudo image is decreasing by increasing the number of angular projections, inserts ambiguity in reconstructed image (Image 39) [34].

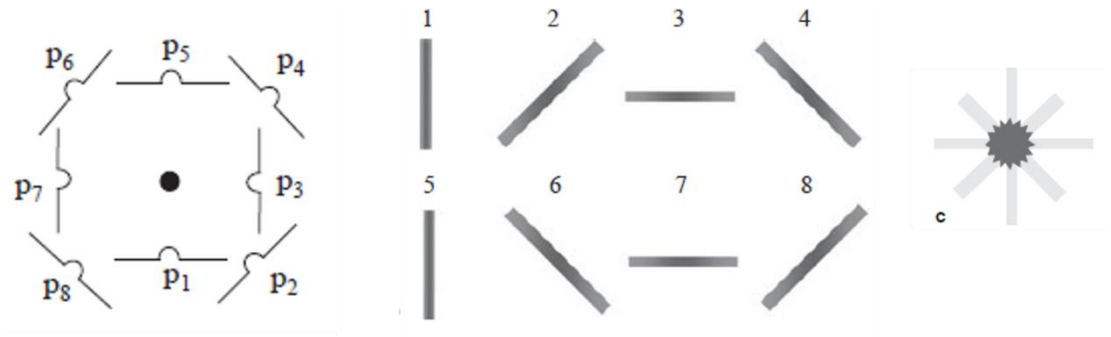

Image 38: Back projection reconstruction [34].

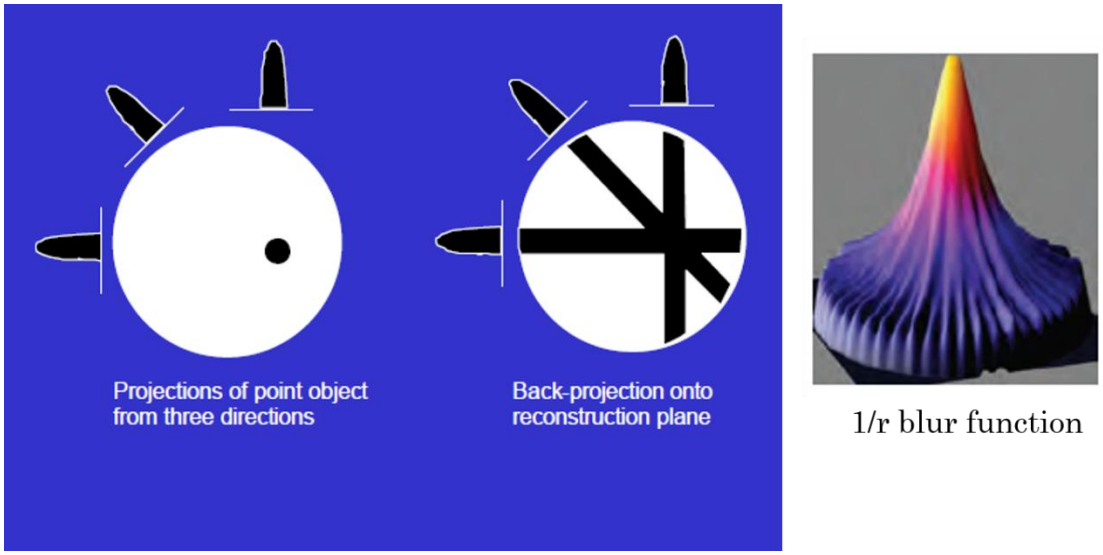

Image 39: Back projection, as a process of summing the projections which come from a large number of angular views (360°) results in blur function 1/r [34].

2.14 Convolution

Convolution is using a “kernel” to extract certain features from an input image. A kernel is a matrix, which is slid across the image and multiplied with the input such is enhanced in a certain desirable manner. The negative values which are inserted around the edges of the projection signal, cancel the unwanted positive signal of ambiguity around its edges of reconfigured image. Choosing the right kernel smoothens or sharpens the edges of the reshaped image (Image 40) [35].

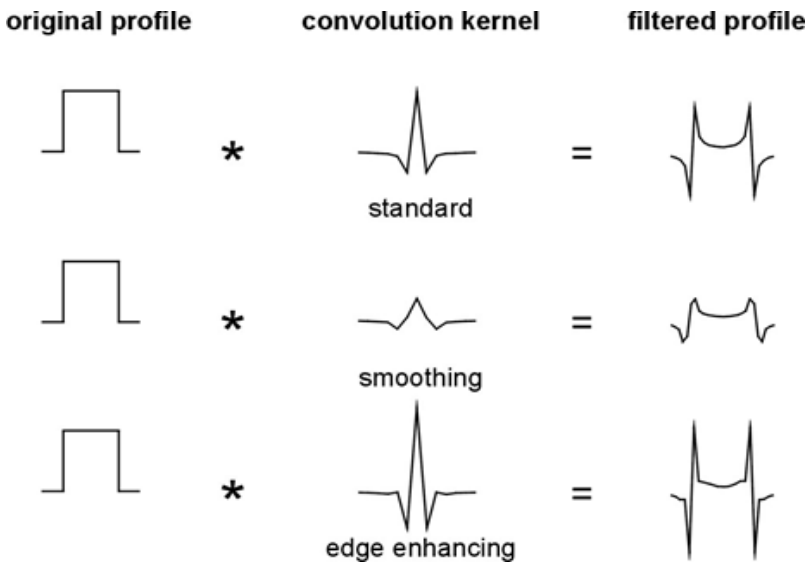

Image 40: Examples of convolution [34].

2.15 Filtered back projection

Filtered back projection is an analytic reconstruction algorithm designed to overcome the limitations of conventional back projection. It applies a convolution filter to remove blurring. It was up until recently the primary method in cross-sectional imaging reconstruction. It utilizes simultaneous equations of ray sums taken at differing angles of a sine wave to compute the values of attenuation coefficients within a cross section [36] (Image 41). Incomplete sampling at high frequencies results in loss of detail information, so the reconstructed images show great ambiguity in their edges (they are blurry) (Image 42). For this reason, the usage of low pass filters can cut high frequencies, which result in insufficient sampling.

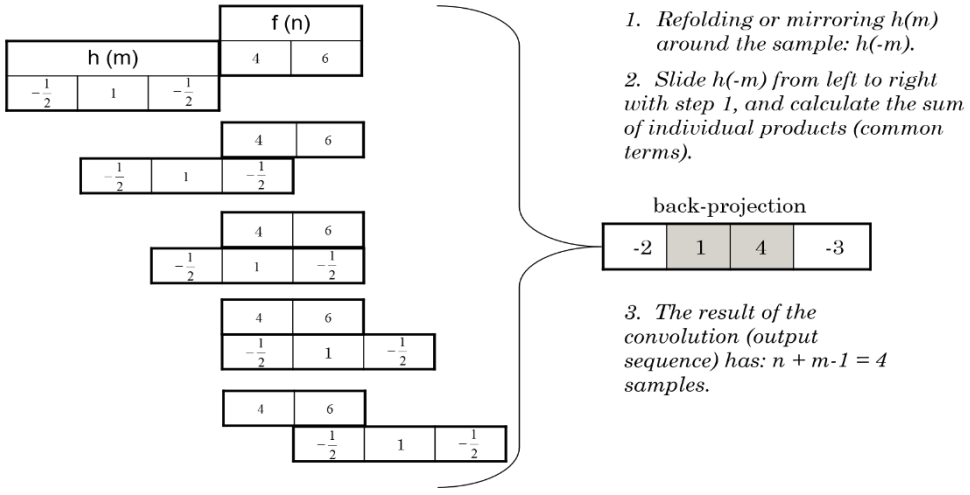

Image 41: Example of filtered back projection [36].

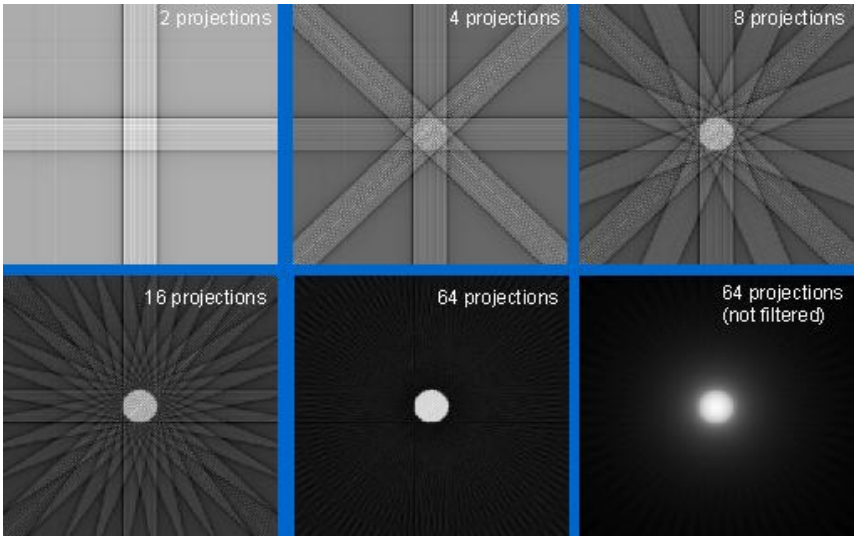

Image 42: Example of sampling effects [36].

2.16 Interpolation effect

Sampling of the 2D FT space is uneven (undersampling in high frequencies), with the sampling density ∞ to 1/|k| (eq. 4), resulting in severe blurring in the reconstructed image.

$$B(k_x, k_y) = \frac{1}{|k|} F(k_x, k_y) \tag{4}$$

1/|k| corresponds to the blur effect in the frequency domain equivalent to the 1/r blurring function of back projection (Image 43).

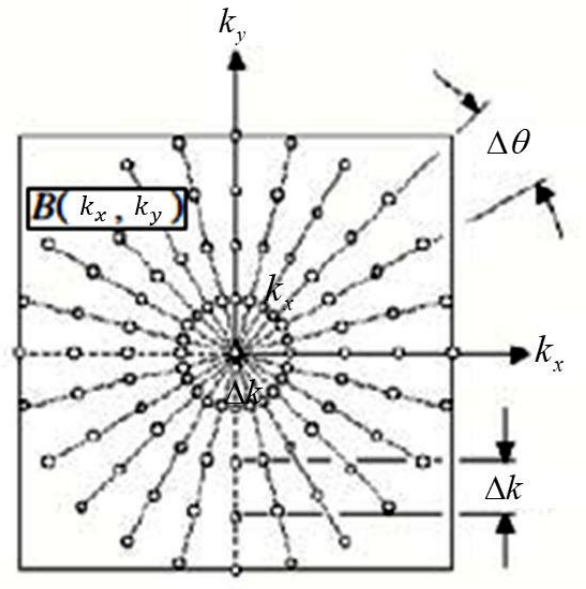

Image 43: Interpolation effect [36].

2.17 Interpolation correction - back projection filters

It is possible to correct the 1/k blurring effect in the frequency domain by multiplying the image by a function, which has an |k| dependency (eq. 5), prior to taking the inverse 2D Fourier Transform of the image (Image 44) (eq. 6). The |k| filter is a starting point in designing a reconstruction filter [37].

$$B(k_x, k_y) = \frac{1}{|k|} F(k_x, k_y) \tag{5}$$

$$thus,$$

$$F(k_x, k_y) = |k| B(k_x, k_y) \tag{6}$$

|k|: corresponds to the ramp filter, introduced to correct blurring.

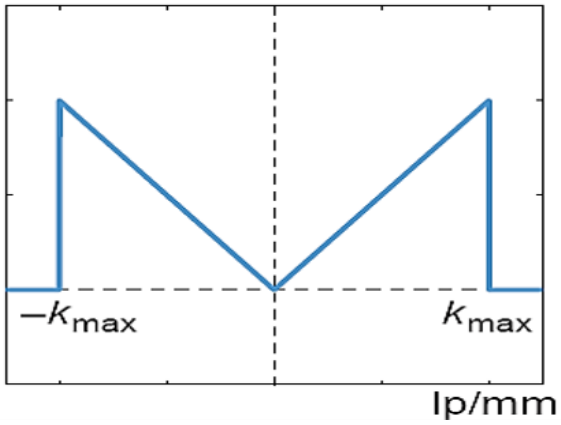

Image 44: Interpolation correction [37].

To limit amplification of high frequencies (quantum noise), the filter function is multiplied by a smoothing function (smoothing window) (eq. 7):

$$H(k) = \begin{cases} \alpha + (1-\alpha)\cos\left(\frac{\pi k}{k_{\max}}\right) & \text{for } |k| < k_{\max} \\ 0 & \text{for } |k| \geq k_{\max} \end{cases} \tag{7}$$

For α = 0.54 Hamming and α = 0.5 Hanning filters are produced respectively (Image 45).

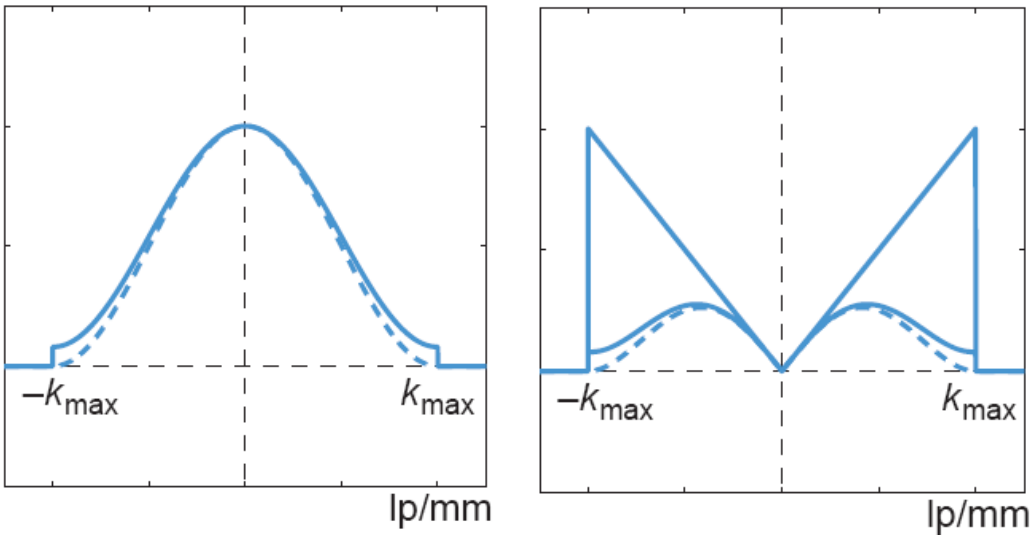

Image 45: Frequency field projection filters, Hamming window (solid line), Hanning window (dashed line) [37].

2.18 Mass attenuation relative to water

The mass coefficient of attenuation of various materials depending on the mass coefficient of water attenuation (Image 46). The value of the “relative” mass coefficient of attenuation increases with an increase of the atomic number [38].

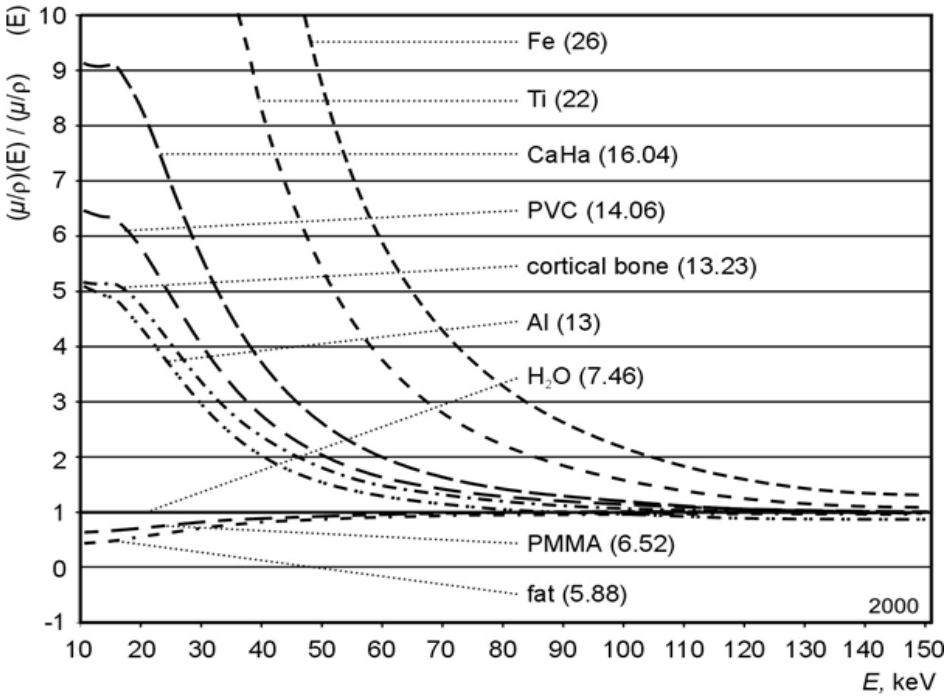

Image 46: Diagram of relative mass attenuation coefficient versus energy (keV) [38].

2.19 The Hounsfield scale

The Hounsfield Unit (HU) scale is a linear transformation of the linear attenuation coefficient measurement into one in which the radiodensity of distilled water (at standard pressure and temperature) is defined as zero HU, while the radiodensity of air at STP is defined as -1000 HU. For a material X with linear attenuation coefficient μ_x, the HU value is therefore given by (eq. 8):

$$HU = \frac{\mu_x - \mu_{water}}{\mu_{water}} \times 1000 \tag{8}$$

where μ_{water} and μ_{air} are the linear attenuation coefficients of water and air respectively.

Each number represents a shadow in the gray scale with +1000 (white) and -1000 (black) at each end of the spectrum. Sensitivity can be increased by decreasing the window width (Image 47) [39].

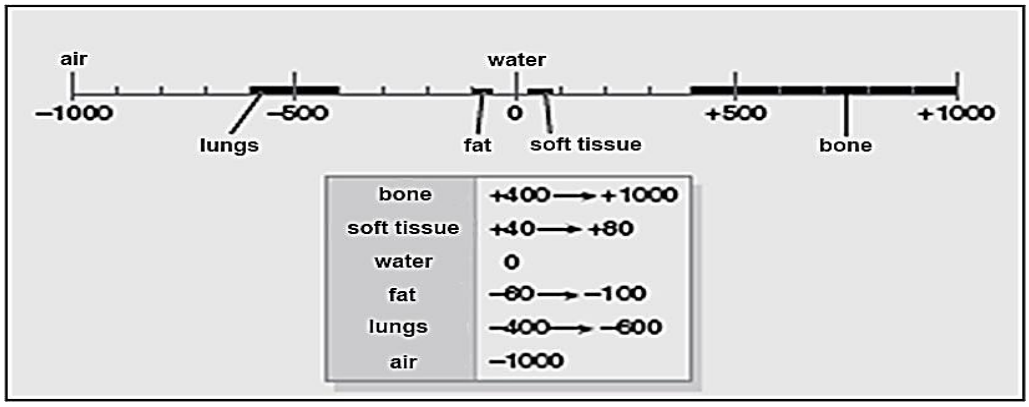

Image 47: The Hounsfield scale [39].

2.20 CT image display

The window function corresponds to a section of the image range (input range) to the available display range (output range) : L = 2^8. The slope determines the degree of amplification (Image 48) [40].

Where the parameters are: window width = r_{max} - r_{min} and level = (r_{max} – r_{min}) / 2 (Image 49) (eq. 9).

$$s = \begin{cases} 0, & r < r_{\min} \\ (L-1)\frac{r - r_{\min}}{r_{\max} - r_{\min}}, & r_{\min} \le r < r_{\max} \\ L-1, & r \ge r_{\max} \end{cases} \tag{9}$$

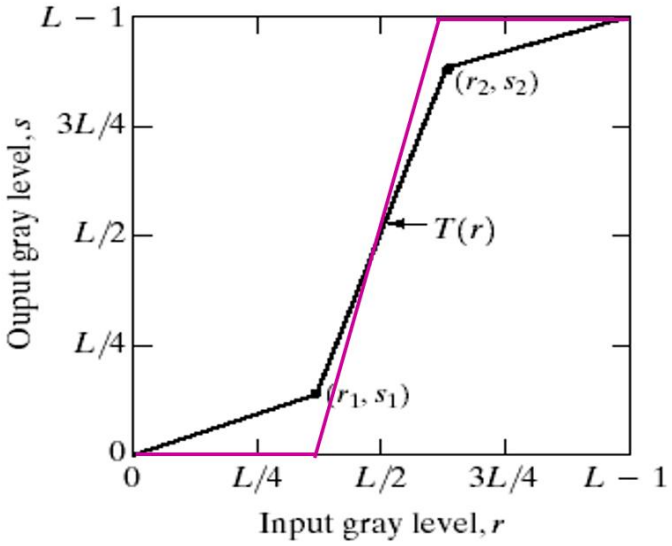

Image 48: Diagram of the output gray level, s versus the input gray level, r [40].

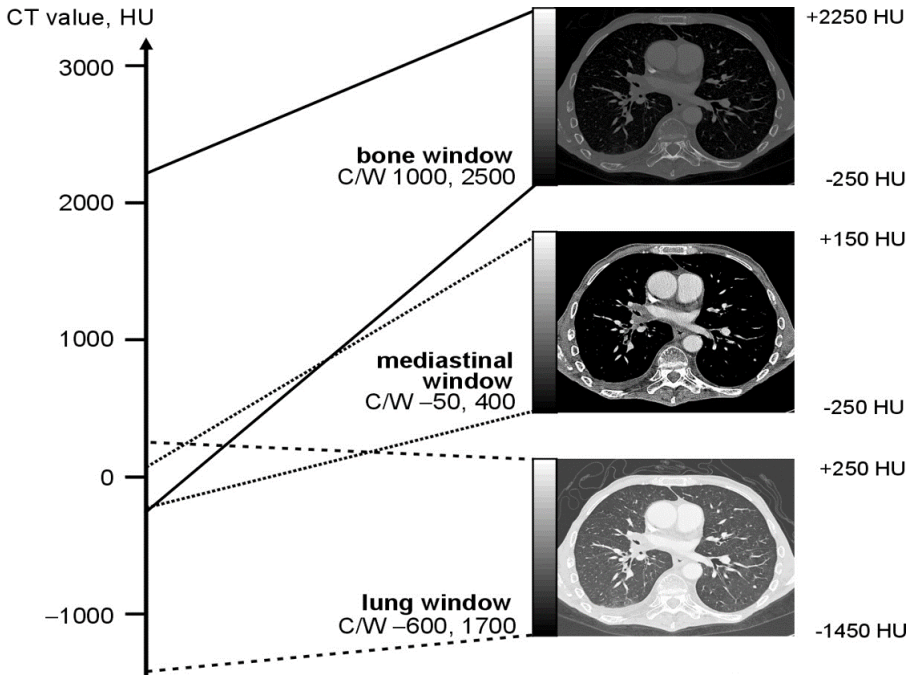

Image 49: Image display on CT: chest window [40].

2.21 Radiation dose and image quality in CT

CT required a high SNR to achieve high contrast resolution and therefore the dose to the slice volume is higher because the used techniques are higher: PA Chest X-ray - 120 kVp, 2 mAs and Chest X-ray – 120 kVp, 200 mAs. Radiation dose is linearly related to mAs. At same kVp and mAs, the number of detected photons increases linearly with the slice thickness, improving the SNR. Larger slice thickness yields better contrast resolution (higher SNR) but spatial resolution in the slice thickness dimension is reduced. Smaller slice thickness improves spatial resolution in slice thickness dimension and reduces partial volume averaging. Noise will increase with thinner slices unless mAs is also increased to compensate for loss of X-ray photons from collimation [40]. In CT, there is a well-established relationship between radiation dose, pixel dimensions Δ, SNR and slice thickness T (eq. 10):

$$D \propto SNR^2 / \Delta^3 T \qquad (10)$$

2.22 Summary: X-ray – CT basic image parameters

The detectability performance can be optimized by balancing between the adjusted protocols parameters (milliampere-second [mAs], peak kilovolt [kVp], slice thickness / pitch and software processing) and tolerated noise and artifacts while maintaining low radiation dose (Image 50).

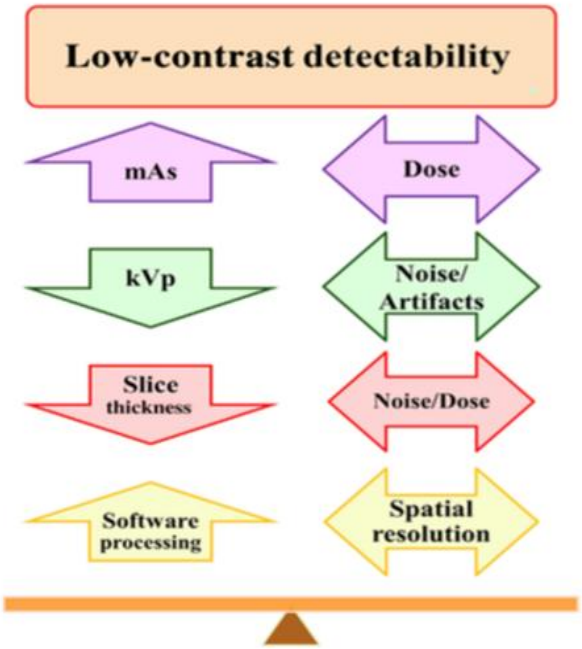

Image 50: Low contrast detectability [40].

Increasing milliampere-second reduces the noise and increases SNR and CNR and as a result LCD is improved. However, increasing milliampere-second increases the radiation dose to the patient (Image 51).

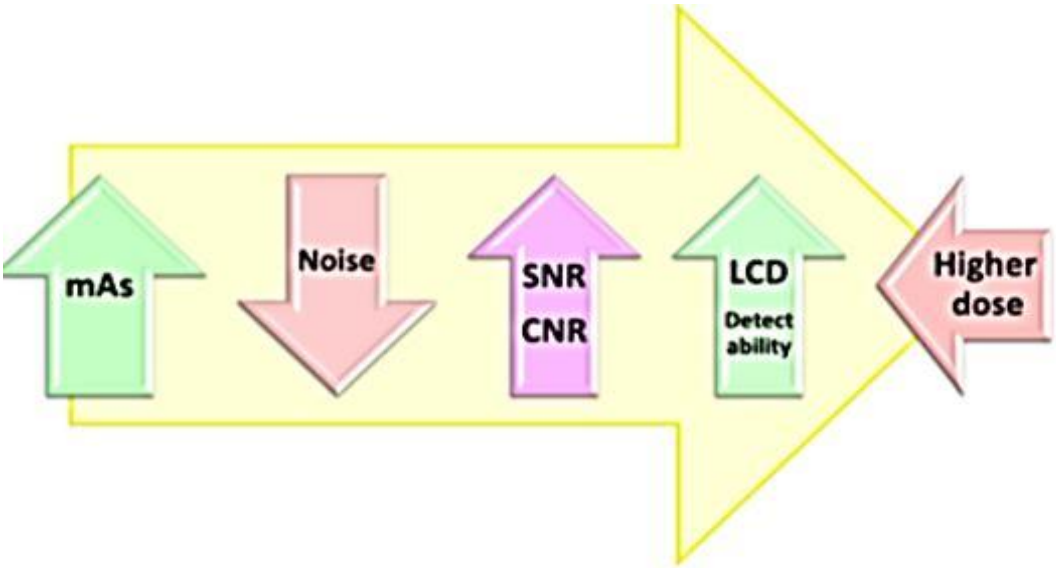

Image 51: The relationship between milliampere-second [mAs], noise, signal-to-noise ratio (SNR) and contrast-to-noise ratio (CNR) and the low-contrast detail (LCD) detectability is illustrated [40].

Appropriately lowering kilovoltage increases photoelectric interaction (PEI) and the attenuation level (AAL), which leads to an increase in SNR and CNR, and hence LCD performance is improved (Image 52). However, the noise level increases with excessively lowering kilovoltage or if the other exposure factors are not adjusted.

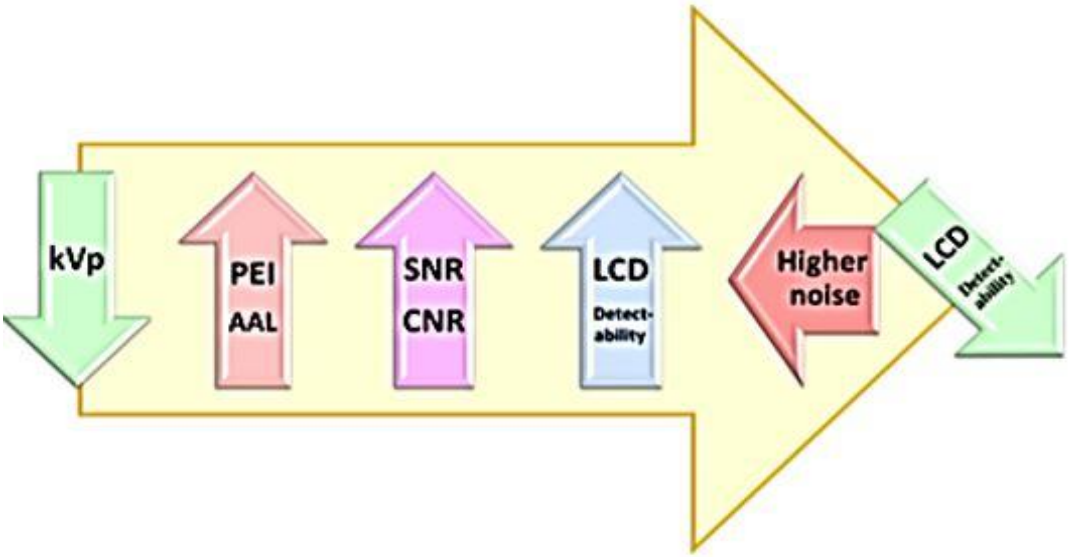

Image 52: The relationship between peak kilovoltage (kVp), signal-to-noise ratio (SNR) and contrast-to-noise ratio (CNR), noise and the low-contrast detail (LCD) detectability is illustrated .

2.23 CT reason of use

The X-ray source/tube typically produces a fan beam spanning the entire subject width. The X-ray source is linked to the detector array in such a way that both can rotate together around the subject. X-rays will be differentially attenuated depending on the types of tissue or media, which come in contact. Tissues or media that strongly absorb X-rays (e.g. bone) appear white while others that absorb poorly of tumor volumes in a genetically engineered mouse model of non-small-cell lung cancer (Image 53) r. The advantages of CT are: the limitless depth of penetration, the high spatial resolution, the good temporal resolution and the clinical utility. The disadvantages of CT are: the poor sensitivity, the primarily anatomical information, the limited soft tissue resolution, the limited molecular imaging applications and the ionizing radiation.

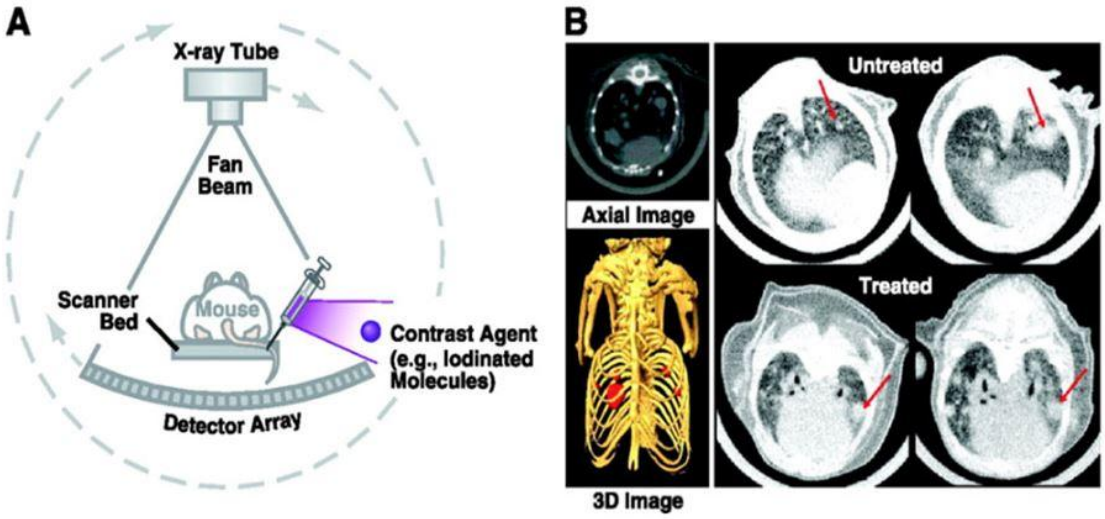

Image 53: A) Illustration of the principles of CT, B) on the left (axial and 3D images) show that lung tumors can be detected via CT (shown in red on 3D depiction), the axial images on the right demonstrate the effects of treating one of these mice with radiation therapy [40].

3. Chapter Nuclear Imaging

3.1 2D scintigraphy

3.1.1 Electromagnetic spectrum

Gamma rays have the smallest wavelengths and the most energy of any wave in the electromagnetic spectrum (Image 54). They are generated by nuclear reactions, like fusion, fission, alpha decay and gamma decay. The wavelength of gamma rays is < 1 nm [41].

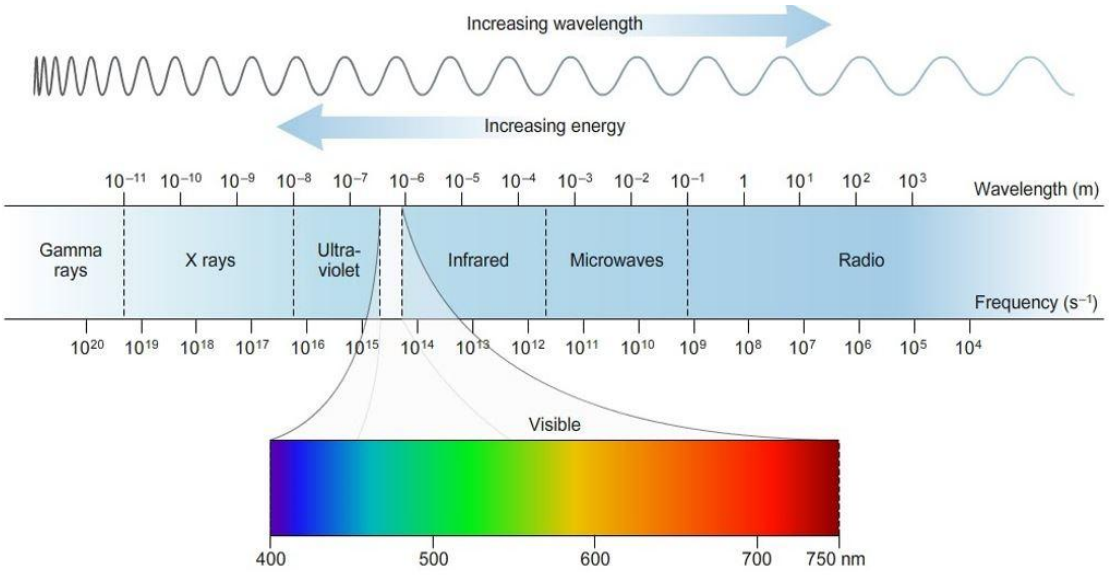

Image 54: Gamma rays in the electromagnetic spectrum [2].

3.1.2 γ-rays emission from radioactive isotopes

The emission of gamma rays does not alter the number of protons or neutrons in the nucleus but instead has the effect of moving the nucleus from a higher to a lower energy state (Image 55). Usually, gamma ray emission follows beta decay, alpha decay and other nuclear decay processes [42].

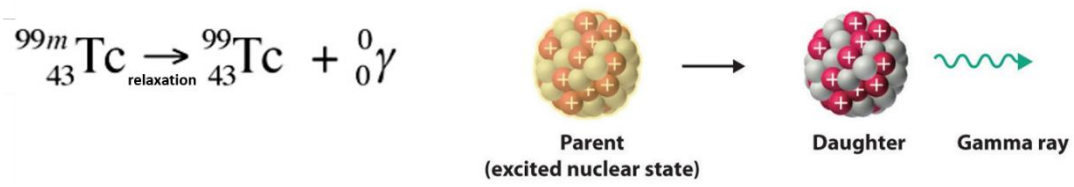

Image 55: Reaction of gamma decay [42].

3.1.3 Main clinical applications

A plenty of SPECT scans are in the field of myocardial perfusion studies, in order to detect coronary artery diseases or myocardial infraction. The result is a single image from a multi-slice data set (typically 100k counts) with a value of spatial resolution ~ 14 mm. Also, SPECT scans are applicable in brain studies to detect areas of reduced blood flow associated with stroke, epilepsy or neurodegenerative diseases / conditions, such as Alzheimer (Image 56). In these studies, the single image is from a multi-slice data set (typically 500k counts) with a value of spatial resolution ~ 7 mm [43].

Table 1: Values of energy E_γ (keV) for each radiotracer.

Radiotracer	Eγ (keV)
Myocardial perfusion (rest/stress)	
^{201}Tl	68 - 80
^{99m}Tc – Sestamibi	140
^{99m}Tc – Tetrofosmin	140
Cerebral perfusion	
^{99m}Tc – HMPAO	140
^{99m}Tc – ECD	140
Oncology	
^{67}Ga	93,185,300
^{201}Tl	68 – 80
^{99m}Tc – Sestamibi	140
Somatostatin receptors: ^{99m}Tc – Depreotide, ^{111}In – Octreotide	140 (^{99m}Tc), 171, 245 (^{111}In)
Labelled antibodies, peptides	

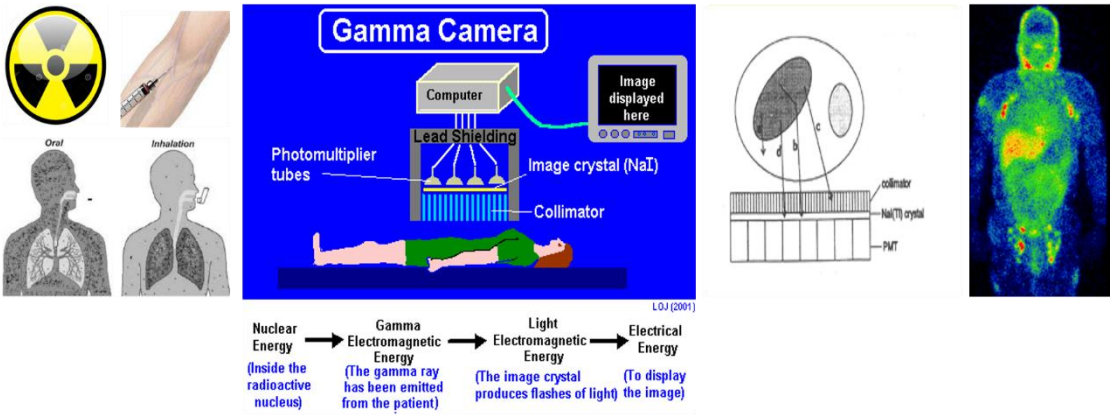

Image 56: The usage of a gamma camera to obtain a nuclear medicine image [43].

3.1.4 How to obtain a Nuclear Medicine image?

Obtaining a nuclear medicine image, the usage of a labeled radionuclide to a pharmaceutical is necessary. The radiopharmaceutical is concentrated in the desired locations, where the nucleus of the radionuclide decays to emit photons and a gamma camera is used to detect these photons.

The parts of a gamma camera are presented (Image 57).

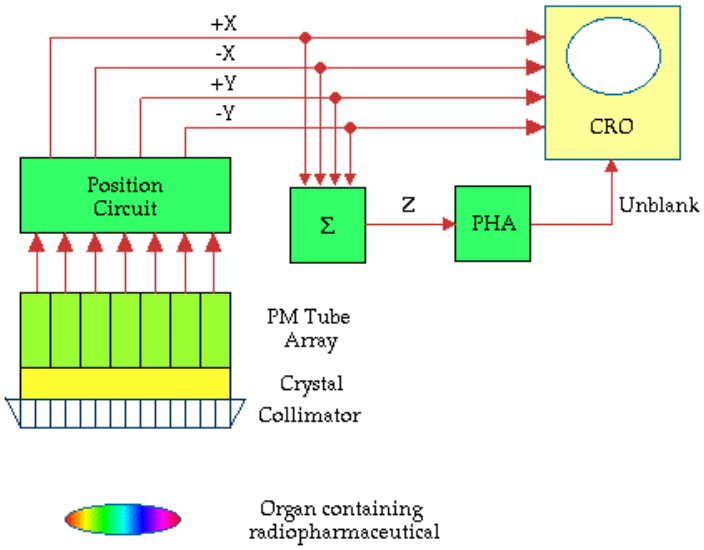

Image 57: Block diagram of a gamma camera [44].

Furthermore, the essential elements of a modern gamma camera are illustrated (Image 58).

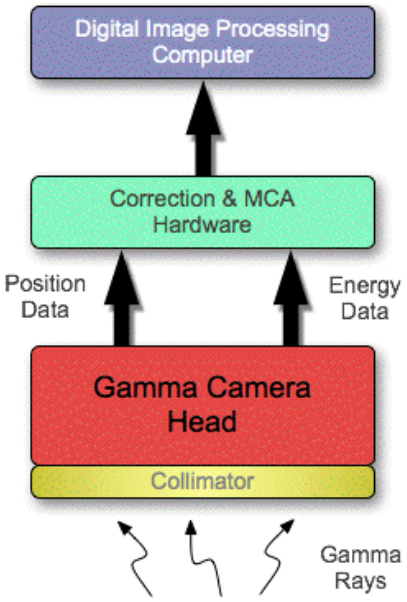

Image 58: A modern gamma camera [44].

The presence of the collimator is to block out all the gamma rays, which are heading to the crystal, except those which are directed at right angles to the plane of the crystal. In the absence of the collimator, these obliquely incident gamma rays would blur the images that produced by the gamma camera. The choice of a specific collimator is dependent on the amount of radiation absorption that occurs (which influences the sensitivity of the gamma camera) and the clarity of the images (that is the spatial resolution) it produces. Unfortunately, these two factors are inversely related in that the use of a collimator which produces images of good spatial resolution generally implies that the instrument is not very sensitive to radiation.

There are three types of collimator: the converging, the diverging and the slant hole (Image 59).

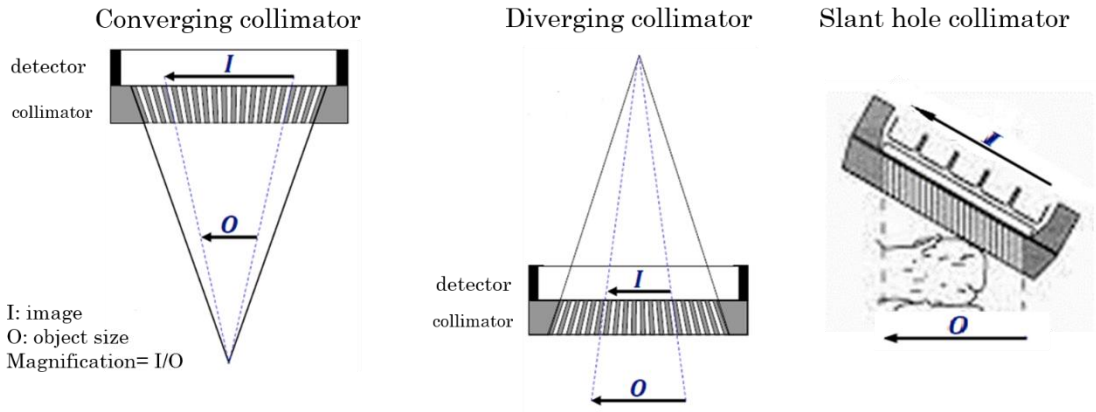

Image 59: The three types of a collimator.

Choosing a suitable collimator is based on the energy of the photons emits the isotope and the desired spatial resolution and sensitivity. In Table 2 are presented the typical examples of parallel hole collimators with geometric characteristics to use for a 40 cm gamma camera [44].

Table 2: Examples of parallel hole collimators with geometric characteristics to use for a 40 cm gamma camera.

Description	Hole diameter (mm)	Number of holes	Septum thickness(mm)
Low Energy High Resolution	1.8	30.000	0.3
Low Energy General Purpose	2.5	18.000	0.3
Low Energy High Sensitivity	3.4	9.000	0.3
Medium Energy High Sensitivity	3.4	6.000	1.4

3.1.5 Scintillator

The scintillator materials are typically inorganic salts such as sodium iodide or cesium iodide that are doped with traces (0.1 mole %) of rare earth materials, such as thallium or cerium (Image 61). Because of the isotropic light emission, the inner surface of the light-tight crystal is coated with a reflective material (TiO_2) so light emitted towards the sides and in front of the crystal are reflected back towards a photomultiplier tube (PMT), this maximizes the amount of light collected and therefore the overall sensitivity of the detector and ensures that the amount of light detected is proportional to the energy of the absorbed photon (Image 60).

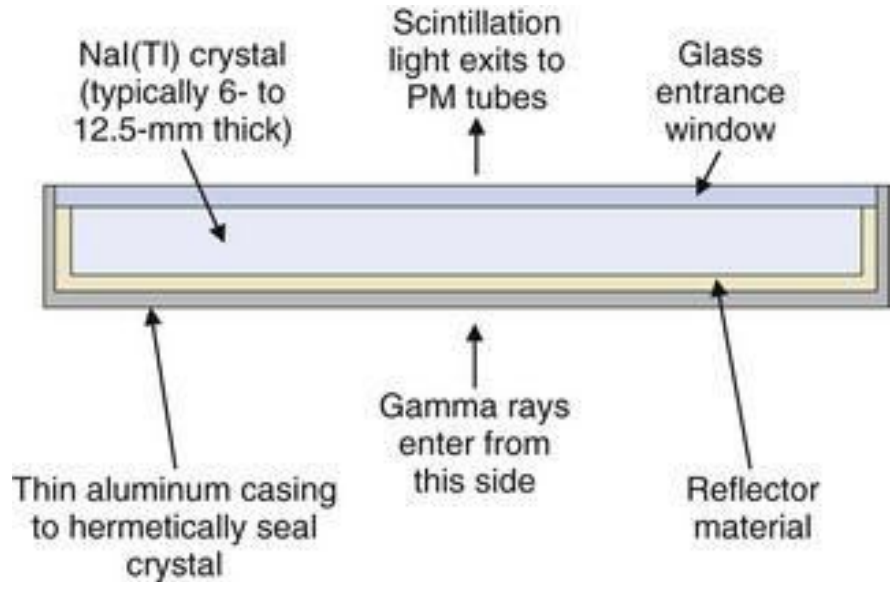

Image 60: A schematic diagram of a scintillator [44].

Image 61: The NaI(Tl) crystal [44].

As the size of the crystal is decreased, the energy resolution typically suffers due to decreased transmission efficiency of the scintillation photons as they undergo multiple reflections along the crystal elements. The small size of the individual crystals (down to ~ 10 μm) can provide good intrinsic spatial resolution, as they provide a natural channeling of the scintillated light (Image 62) [44].

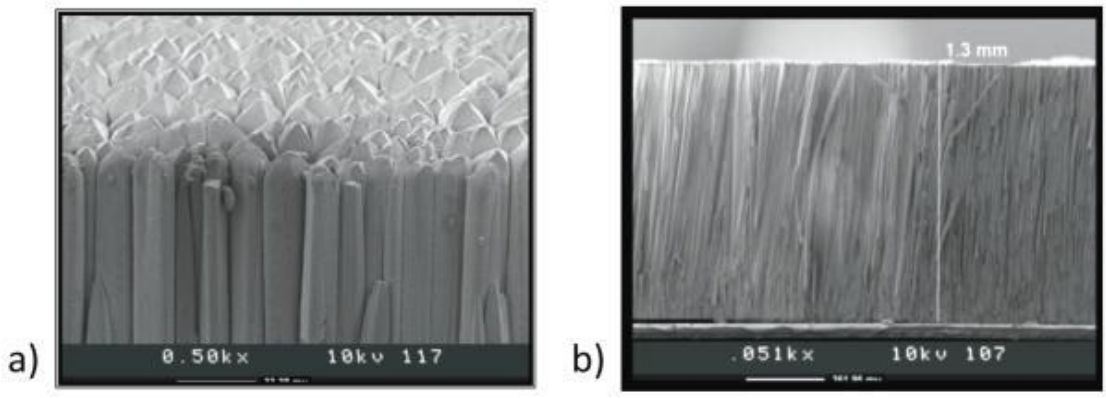

Image 62: a) Top and b) cross-sectional SEM micrographs of a 1.3 mm thick micro-columnar CsI(Tl) film [44].

3.1.6 Optical coupling

The light pipe is interposed between the back of the crystal and the entrance window of the PMT and is a thin layer of transparent optical gel. The light pipe

optically couples the crystal to the PMT and thus maximizes the transmission of the light signal (90%) from the crystal into the PMT (Image 63). Lack of a proper thickness of the light guide on the gamma camera can ruin the accuracy of estimated position on the gamma camera. In addition, both the linearity and uniformity responses have a strong dependency on the thickness of light guide. The optimum light guide thickness for the ideal value of linearity is approximately equal to the effective radius of the PMTs. It has been shown that the depth of interaction of gamma radiation in crystal has an impact on the full-width at half-maximum (FWHM) of the light spread function [45].

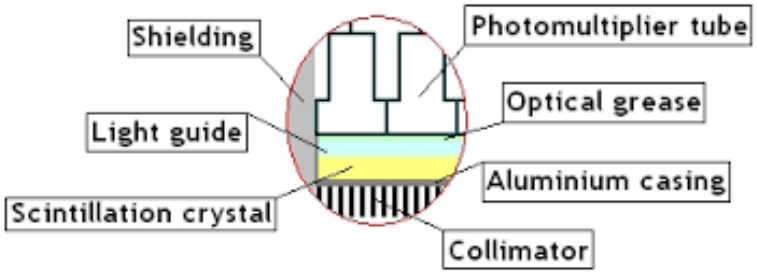

Image 63: Schematic drawing of a gamma camera [45].

3.1.7 Photomultipliers

A photomultiplier is a photo-emissive device, where the absorption of a photon results in the emission of an electron. It is useful for the detection of light of very weak signals. These detectors work by amplifying the generated electrons by a photocathode, which is exposed to a photon flux (Image 64, Image 65). Usually, an array of 61, 75 or 91 PMTs are used to cover the large crystal area. The most efficient geometry is the hexagonally-close pack, where the distance from the center of one PMT to the center of each neighboring PMT is the same and this fact is important to reconstruct the position of the scintillated event [46].

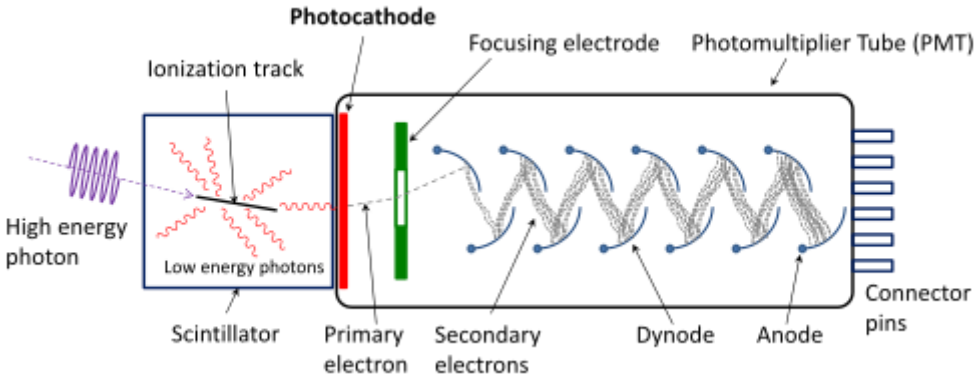

Image 64: Schematic drawing of a photomultiplier [45].

Image 65: A picture of a photomultiplier [45].

3.1.8 Energy resolution

In a gamma camera, the energy resolution is defined as FWHM of a photopeak, where for the narrower value of FWHM, the better is the ability of gamma camera in discrimination of un-scattered and scattered gamma rays. The typical energy resolution value without a patient is 14 keV, which is equivalent to 10% and measured during calibration. In presence of a patient,

the typical energy resolution value is 28 keV = 20% (Image 66), setting at this value to increase the acceptance window [47].

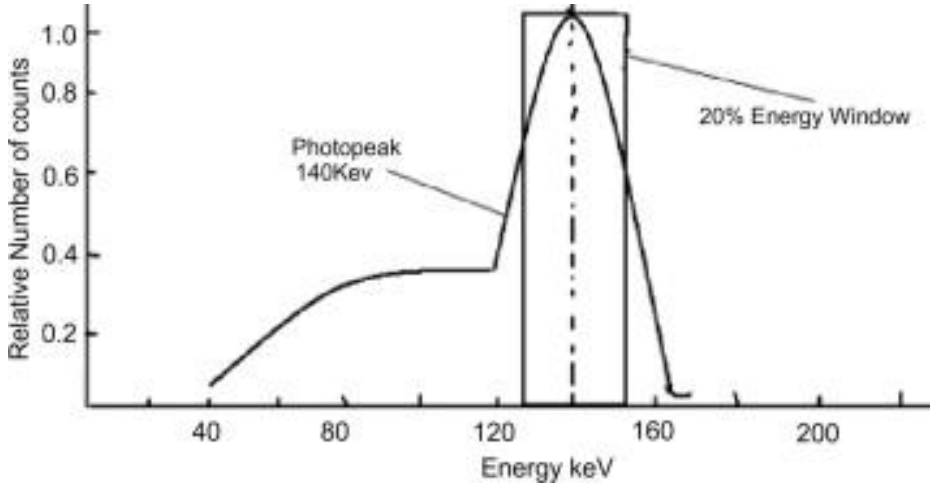

Image 66: Diagram of the relative number of counts versus the values of energy of Tc-99m (keV) [47].

3.1.9 Detection efficiency

The detection efficiency of a gamma camera is defined as the fraction of emitted gamma rays that produce counts in the image. The detection efficiency of E_{camera} is defined as (eq. 11):

$$E_{camera} = G \bullet \varepsilon \bullet f \quad (11)$$

where G is the collimator's contribution (geometric collimator efficiency), f is the read-out contribution (fraction of photons accepted by energy discriminating unit) and ε is the scintillator's contribution (ratio of gamma rays recorded by the scintillator N_{record} to the gamma rays hitting it N_{hit}) (eq. 12),

$$\varepsilon = \frac{Nrecord}{Nhit} = 1 - e^{(-\mu * d)} \quad (12)$$

where μ is the scintillator's linear attenuation coefficient at $E_{\gamma,}$ d is the scintillator thickness (Image 67) [48].

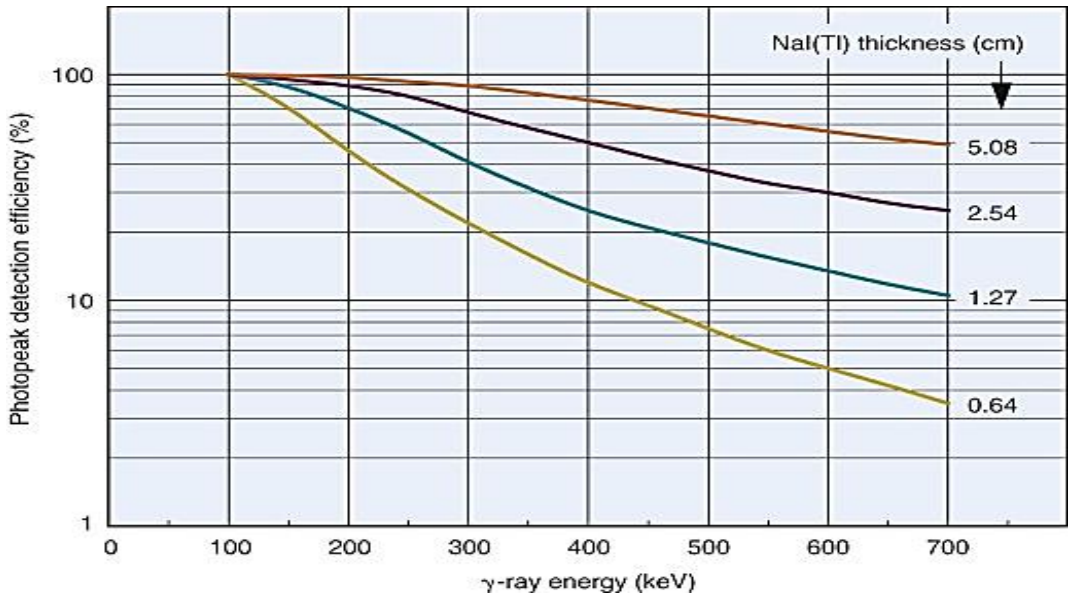

Image 67: Diagram of the photopeak detection efficiency (%) versus the values of gamma ray energy (keV) [48].

3.1.10 Spatial resolution

The total spatial resolution of a gamma camera, δrtot is defined as (eq. 13):

$$\delta rtot = \sqrt{\delta r^2_{coll} + \delta r^2_{int} + \delta r^2_{Compton}} \quad (13)$$

where δrcoll is the spatial resolution of the collimator, δrint is the gamma camera's intrinsic resolution and δrCompton is the Compton scattering contribution. The typical values of overall spatial resolution are: 1-2 cm deep in the body and 5-8 cm close to surface of the body (Image 68) [49].

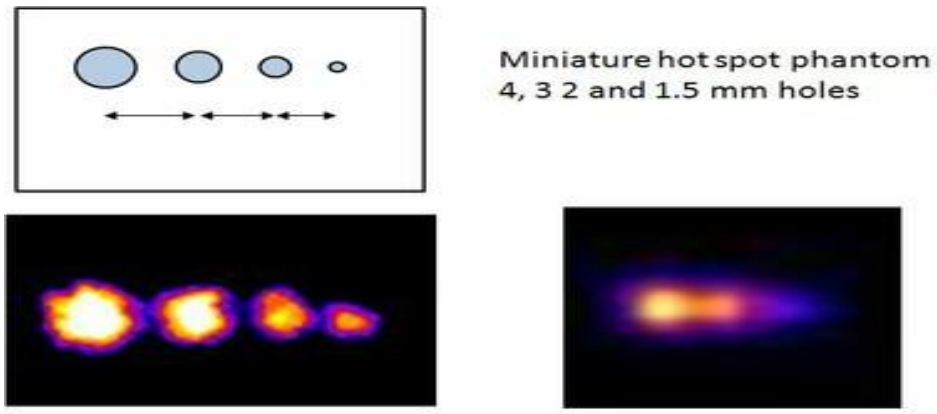

Image 68: Example of spatial resolution of a gamma camera [49].

3.1.11 Dead time

The dead time τ is defined as (eq. 14):

$$\tau = \frac{N - n}{nN} \tag{14}$$

where N is the true count rate that is the number of scintillations per second and n is the measure of count rate.

The maximum measurable count rate is 1/τ and the dead-time corrections are based on the calibration using phantoms of known radioactivity. The camera cannot produce further pulses during the dead time and only produces pulses of lesser height until the recovery time has elapsed (Image 69) [50].

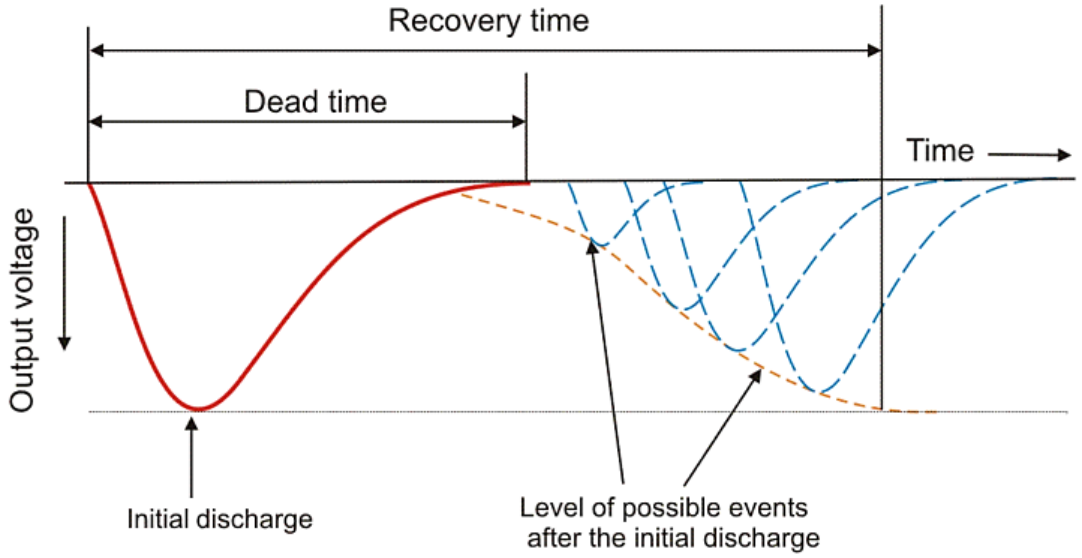

Image 69: The definition of dead time [50].

3.1.12 Signal to Noise Ratio (SNR)

The radioactive decay is a statistical process, where the number of disintegrations per unit of time fluctuates. The Poisson distribution shows that the SNR depends on number of detected gamma rays N, SNR ∝ N (Image 70). The factors, which are affecting the SNR are: the administered radioactivity, the radiotracer uptake, the depth of organ in body, the total scanning time, the intrinsic resolution of gamma camera and the post-acquisition filtering [51].

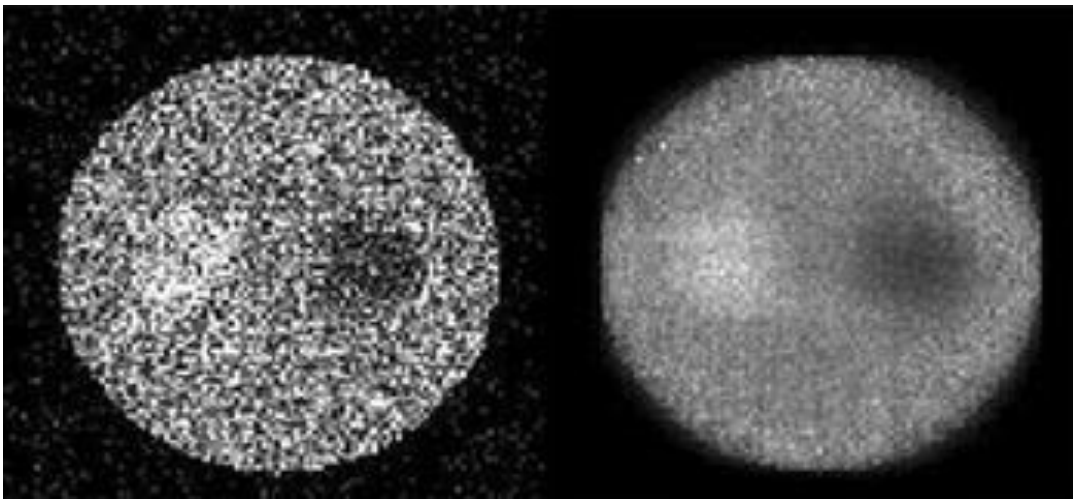

Image 70: High SNR (left), low SNR (right) [51].

3.2 SPECT

3.2.1 SPECT scanner components

A SPECT scanner is consisted of two or three gamma cameras (heads), where multiple heads systems acquire multiple views simultaneously (Image 71), a converging collimator, which often is used inside the gamma cameras to increase the SNR and the moving bed. The heads can be placed at different angles and positions and are moved in and out to make the distance from the instrument under study as close as possible, outwards to accommodate the body and inwards to bring the gamma cameras close to the brain [52].

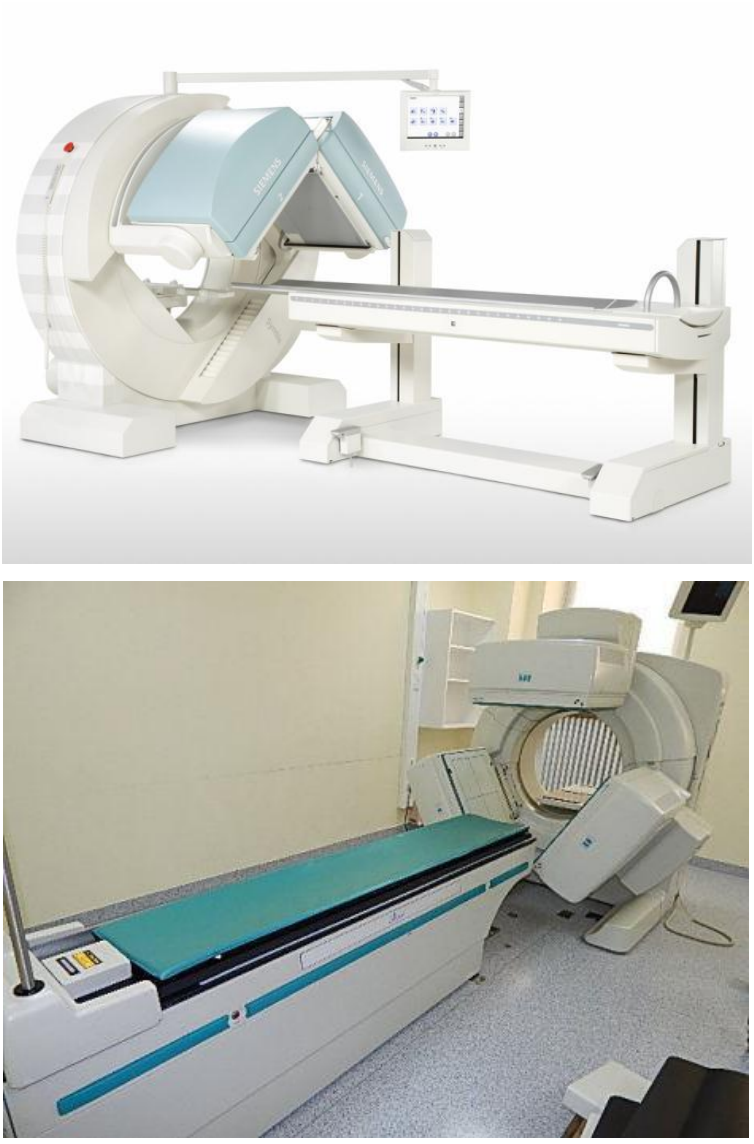

Image 71: A SPECT scanner with two heads (up) and three heads (down) [52].

3.2.2 Data acquisition

The rotation of gamma cameras around the patient depends on the different thickness of body in FOV, using different source-detector distance at different positions. That affects the degree of tissue attenuation, the distribution of gamma rays in body and the spatial resolution due to the diverging-cone shape of line of response defined by the collimator, as a result the projections at 180^{o} to each other are not identical and the 360^{o} rotation, which is known as conjugate counting needed, combines data acquired from opposing views, reduces the attenuation effects and gives uniform resolution (Image 72). For the image formation are used two methods: the scatter correction method and image reconstruction [53].

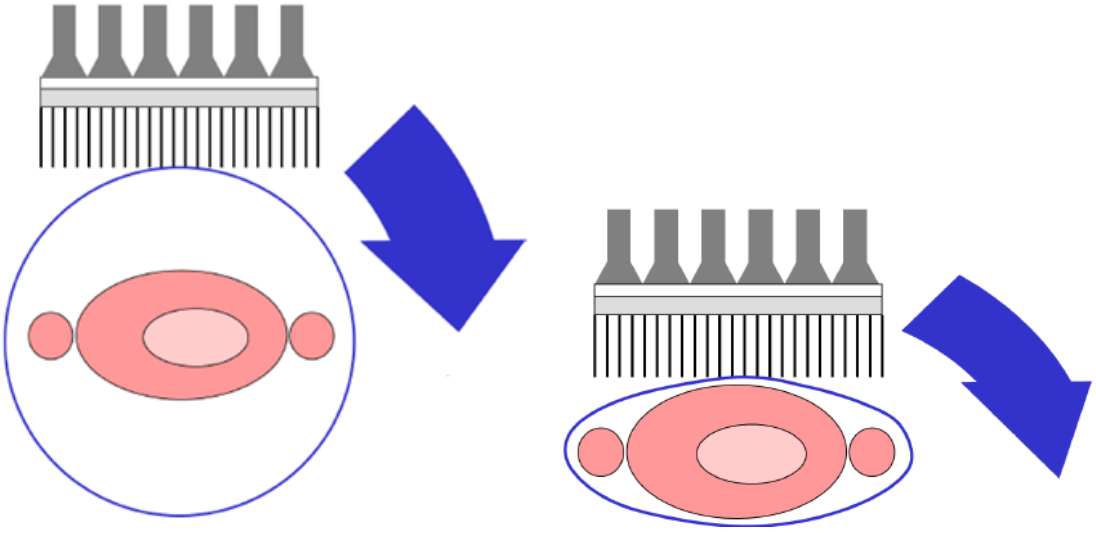

Image 72: Illustration of circular orbit (up) and contoured orbit (down) [53].

3.2.3 Attenuation

The gamma rays are directed from radiotracer inside body through the patient to get to the detector, so the attenuation is observed. The attenuation depends on the amount of tissues that gamma rays go through and the gamma rays with low energy are more attenuated. The measurements of a SPECT scanner concern to the distribution of radiotracer and not to the attenuation, because the attenuation creates artifacts, which need correction. Three methods have been developed to correct the attenuation (Image 73), one empirical (shape and attenuation of an average patient is used) and two analytical methods (Chang's multiplicative and transmission scan) [54].

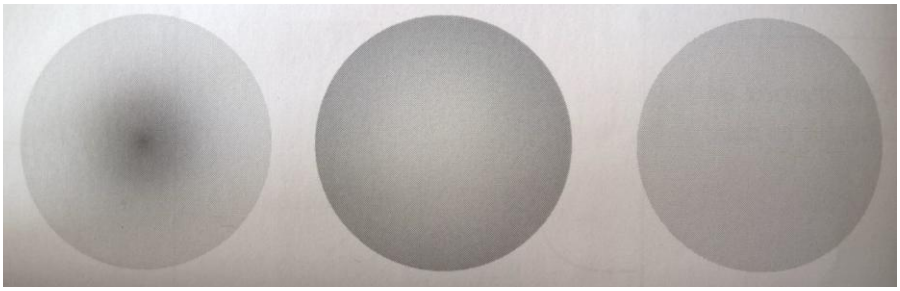

Image 73: Illustration of an uncorrected image (left), corrected attenuation (center) and corrected image (right) [54].

3.2.4 Image reconstruction

SPECT uses CT techniques to reconstruct 2D axial slices from acquired projections and 3D distributed radionuclides. Two types of algorithms for

reconstruction are used: the filtered back-projection techniques, which are identical to CT and the iterative techniques, where methods/algorithms are developed to speed it up, including the use of a subset of acquired profiles. The most common iterative algorithm is the maximum-likelihood expectation maximum method (Image 74) (ML-EM) [55].

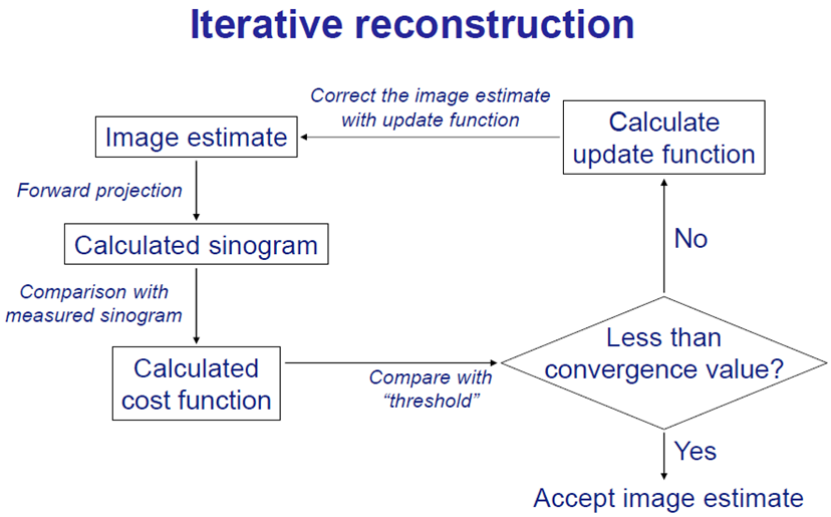

Image 74: Flow chart of iterative reconstruction [55].

3.2.5 SPECT reason of use

The advantages of SPECT are the limitless depth of penetration, the opportunity to image functions of the body (e.g. heart blood perfusion), good sensitivity, multiplexing capabilities, and the clinical utility (Image 75). On the other hand, the disadvantages of SPECT are: the high cost, the ionizing radiation, the limited spatial resolution and the lack of attenuation correction [56]. Attenuation correction can be found on SPECT-CT systems.

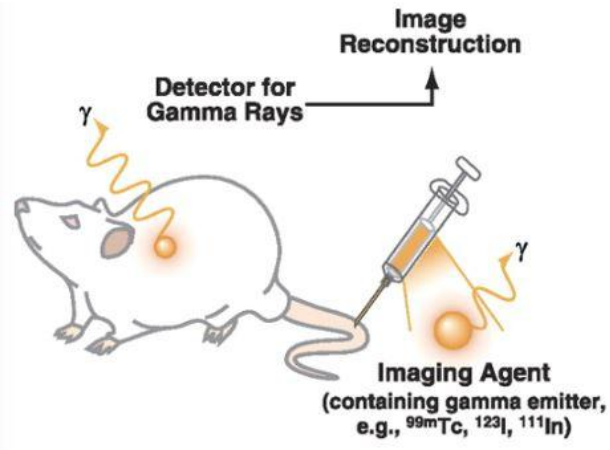

Image 75: The principles of SPECT [56].

3.3 PET

3.3.1 PET scanner components

The Positron Emission Tomography (PET) scan is an imaging technique, which uses radioactive molecules to create an image of internal tissues and organs. This type of scanner is useful in detecting cancer cells because the tumors have a different color than surrounding healthy cells. The PET scanner is similar to the CT scanner and its components are the gantry, the subject table, the detector/camera system and a computer system (Image 76) [57].

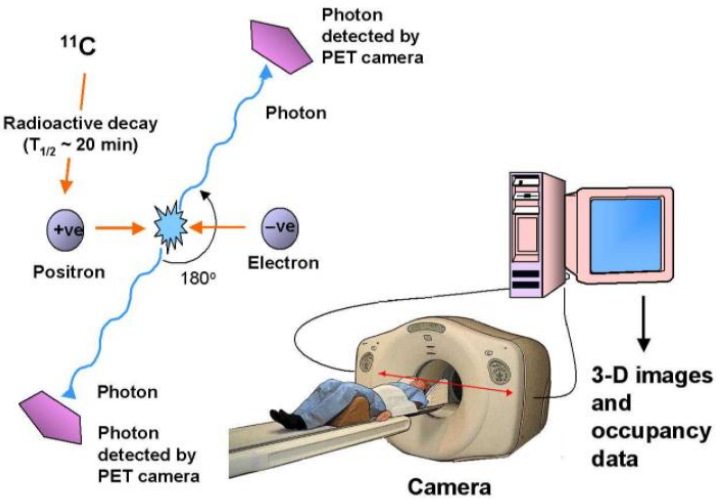

Image 76: Diagram of the components of a PET scanner [57].

3.3.2 Data acquisition

The sinogram is a method of storing and viewing raw PET data. In the sinogram, the LOR is plotted as a function of angle of orientation versus the shortest distance between the LOR and the center of the gantry. There is a sinogram for each slice and it contains the projection data across all projection angles [58].

3.3.3 Image formation

Tomographic reconstruction methods are used to form volumetric images. The correction of raw data is focused on random coincidences, estimation and subtraction of scattered photons, detector dead-time correction and detector sensitivity correction. Filtered back projection has been used to reconstruct

images. The Shepp-Vardi algorithm is now the preferable method for reconstruction [59].

3.3.4 Scatter correction method (Event detection within pair production time window “collimator” for PET)

The energy-based scatter-correction techniques are used in commercial PET scanners, which store the energy information for the photon pair. The assumption of multiple energy-window methods gives a number of windows below and above the photopeak window, estimating either the complete energy spectrum of the scattered counts or at least the integral of that spectrum from the lower energy discriminator of the photopeak window to the upper energy discriminator of that window [60].

3.3.5 Attenuation

The attenuation correction is required in quantitative PET imaging and is based on a transmission scan using ^{68}Ge rotating rod source. The values of attenuation are measured at 511 keV. The attenuation effect exists when photons emitted by the radiotracer inside the body are absorbed by intervening tissue between the detector and the emission of the photon. The structures deep in the body are reconstructed as having incorrectly low tracer uptake [61].

3.3.6 PET reason of use

The benefits of PET scan are the great diagnostic clarity because of the large sensitivity because of the absence of collimator, showing areas of increased activity within the body. Areas that their function is correlated with the radiopharmaceutical that has been used. PET scan is a painless and fast procedure, measuring both anatomy and metabolic function in a single scan. Disadvantages of PET is the time need for each imaging procedure and as in every procedure that ionizing radiation is used, it cannot be used in pregnant women and diabetics.

4. Imaging in vivo experiments

4.1 The mouse as a preclinical model

Over the past century, the mouse has evolved into a leading mammal model for in vivo research. Scientists from a wide range of biomedical fields have chosen the mouse because of its close genetic and physiological resemblance to humans, as well as the ease with which it can manipulate and analyze its genome. Most common research application using the musculus model is drug discovery. During the development of new drugs, a large number of compounds are produced in order to identify the most promising candidates for further development (Image 77). Promising candidates,

generally related to structure, are often selected using in-vitro test models. Candidates who were not rejected in these initial evaluations are then tested for efficacy and safety in animals, usually rats and mice. These animal studies are designed to allow the selection of a safe initial dose for humans (including the assessment of safety margins between clinical and toxic doses), to predict pharmacokinetic / pharmacodynamics. Animal studies can provide essential evidence for the effectiveness of the product [62, 63].

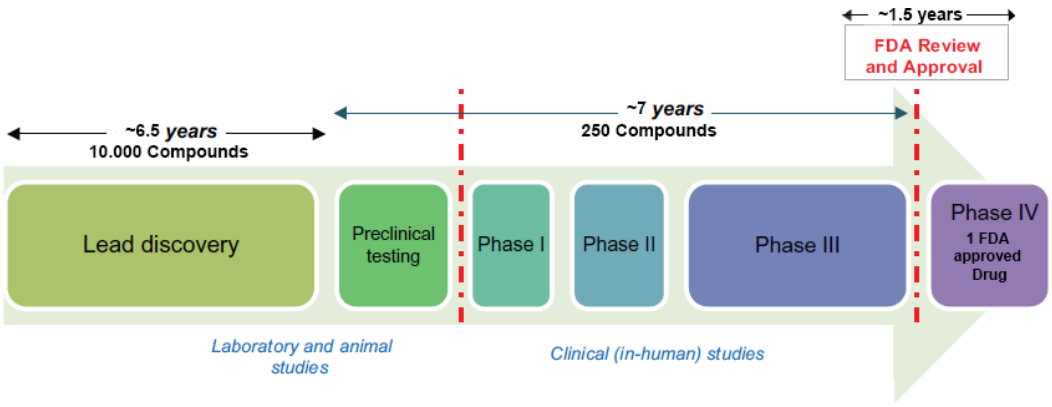

Image 77: Drug discovery and development phases relative to time and compound number [62].

4.2 In vivo experiments

In vivo experiments took place at BIOEMTECH Laboratories (Athens, Greece) in order to give an altogether view of the imaging techniques which have been discussed previously. Injections from different administrations routes were performed, using the optimal form of anesthesia (isoflurane), causing minimal stress to the animals (Image 78).

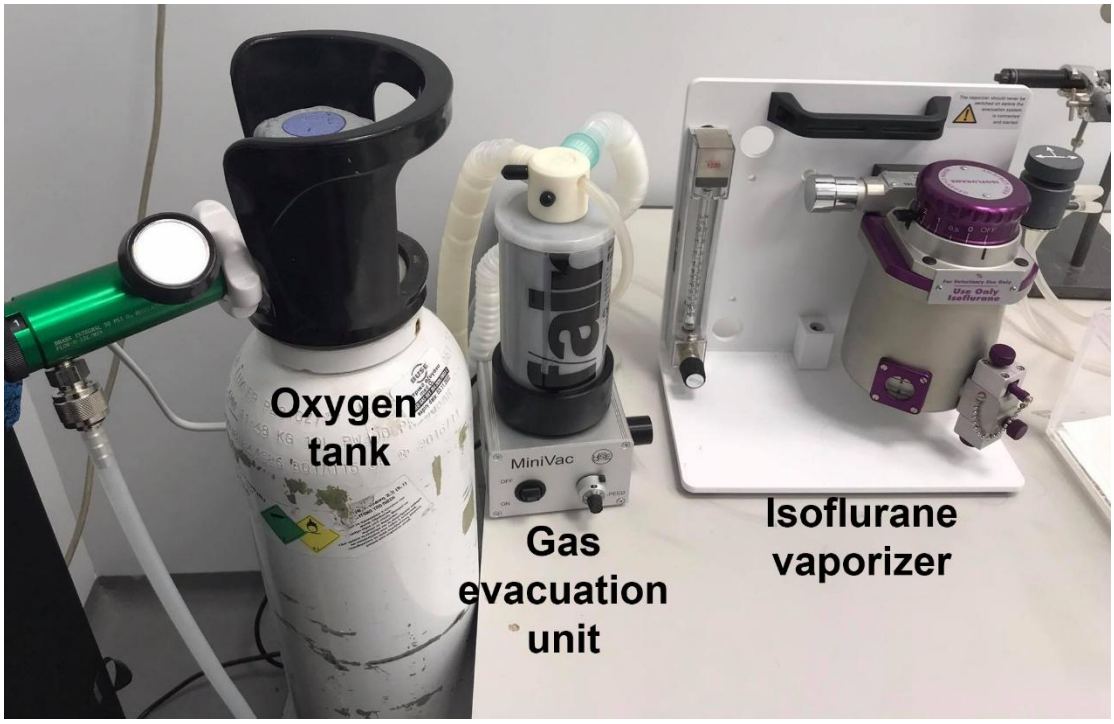

Image 78: Anesthesia station.

4.3 The in vivo infrastructure of these projects

4.3.1 Planar imaging

Real-time, static screening was performed on γ-eye™(Image 81) and b-eye™ (Image 80) (BIOEMTECH, Greece) and post processing on its embedded analysis software, visual|eyes™. X-ray procedures were performed on a custom made system developed by BIOEMTECH (Image 79).

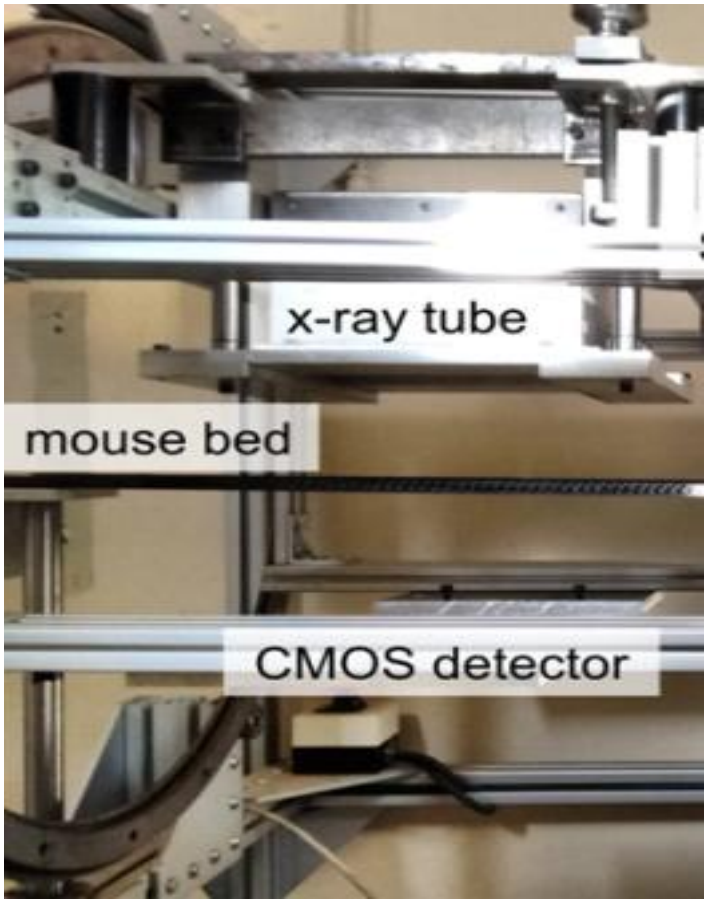

Image 79: The developed X-rays system consists of an X-rays tube and a CMOS detector, mounted on the rotating gantry and separated by a distance of 30cm, to allow whole body imaging in a single shot.

Image 80: b-eye™ β-eye is a unique benchtop system, suitable for whole-body coincidence mouse imaging. It provides static and fast dynamic images with user-selection time frame.

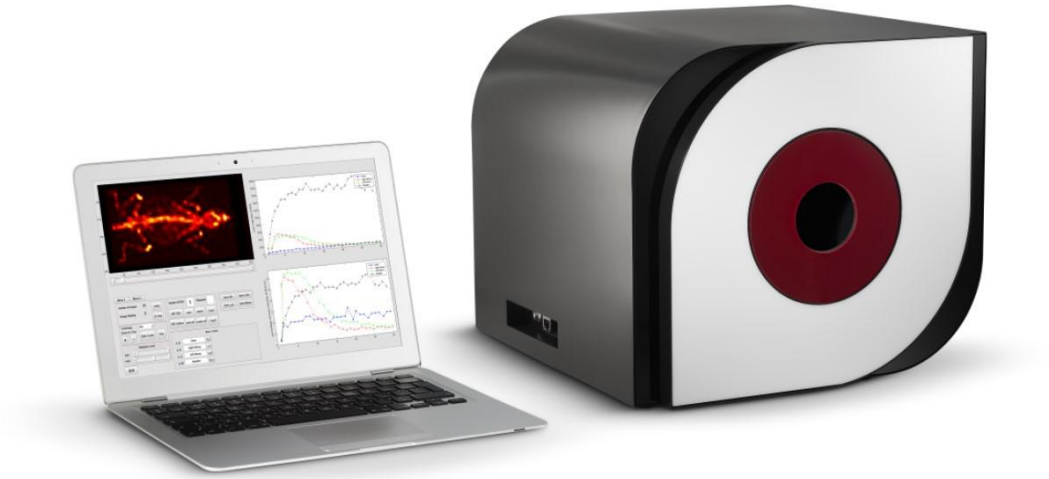

Image 81: γ-eye is a unique benchtop system, suitable for whole-body scintigraphic mouse imaging. It provides static and fast dynamic images with user-selection time frame.

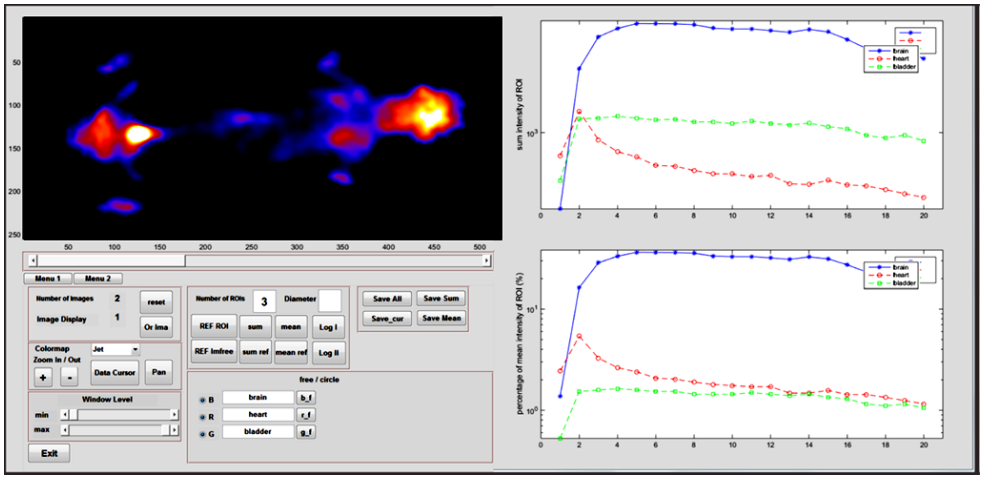

Image 82: The visual|eyes software supports a real-time viewer mode with selectable time frame as well as a post processing mode, where various tools are adapted.

4.3.2 Tomographic imaging

Tomographic SPECT/CT imaging was performed on X-CUBE (Image 83) /γ-CUBE (Image 84) (Molecubles, Belgium) and post processing on VivoQuant (Invicro, Boston).

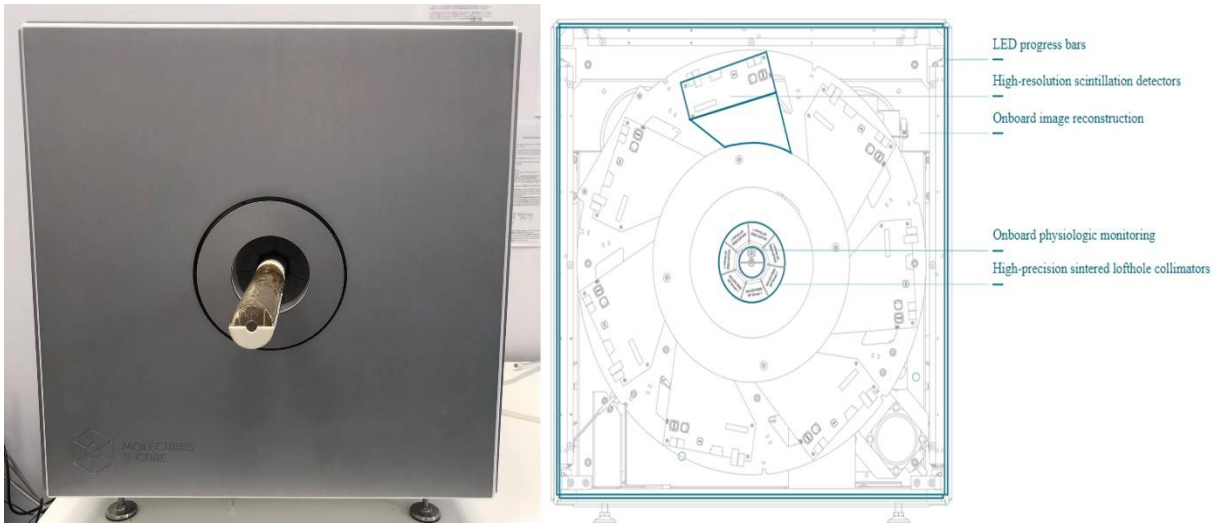

Image 83: The γ-CUBE is a high-sensitivity, high-resolution SPECT imager allowing whole-body mouse and rat imaging.

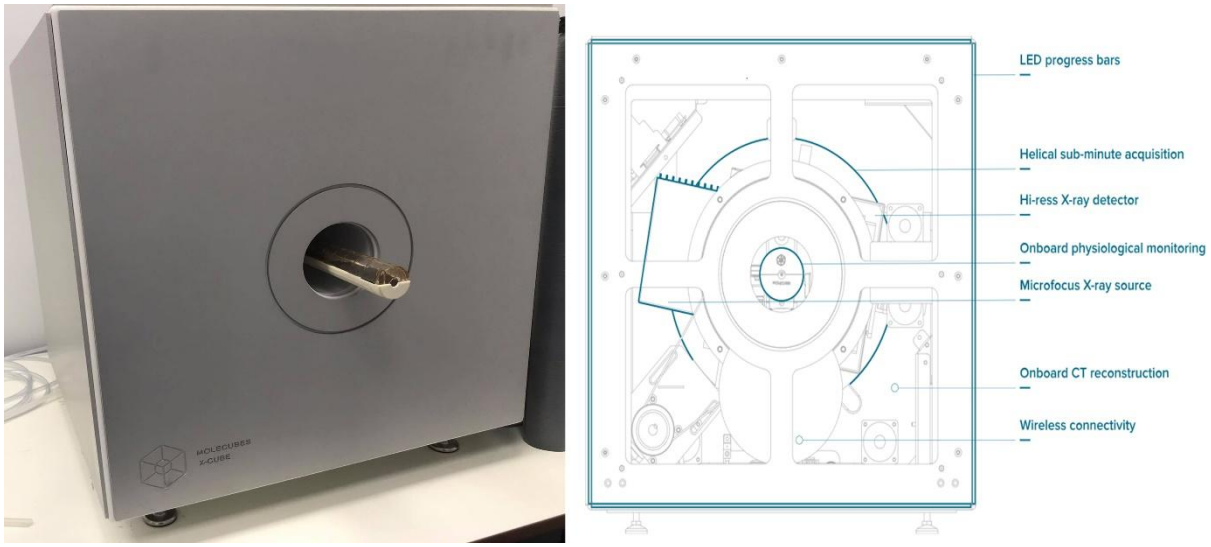

Image 84: The X-CUBE is a high throughput CT system. It allows for fast total body mouse and rat CT imaging at extremely low dose and great soft tissue contrast.

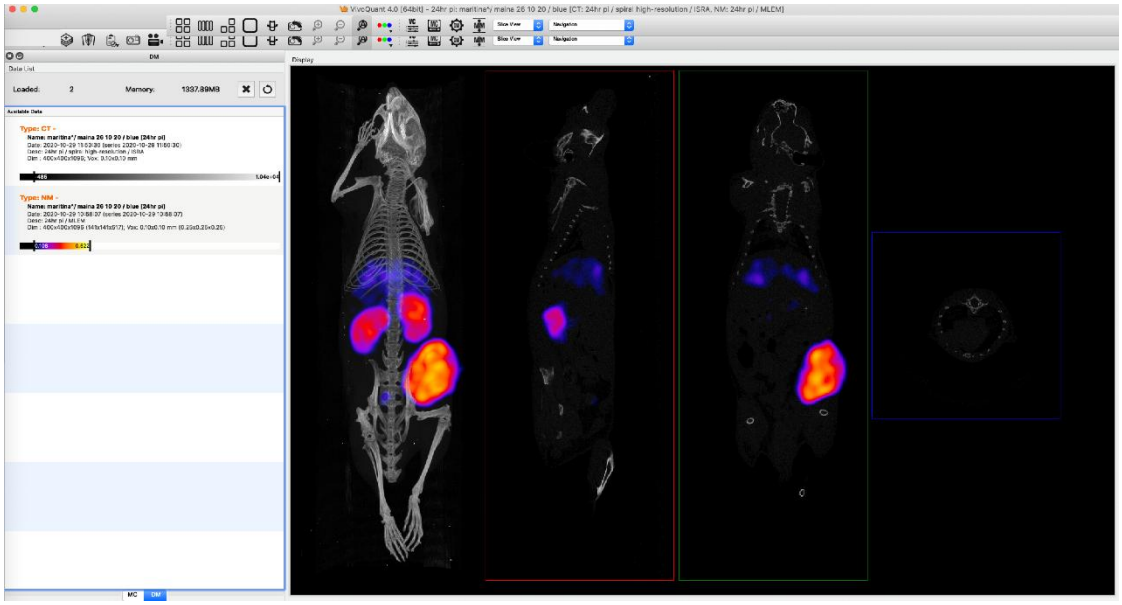

Image 85: VivoQuant™ is Invicro's multi-modality post-processing suite for SPECT, CT imaging data.

4.4 X-ray and CT experiments

Some proof on concept experiments were performed on the planar X-Ray imaging system in BIOEMTECH Laboratories. More specifically, gold nanoparticles (AuroVist, Nanoprobes, 15nm) were injected i.v. in healthy mice, in different concentrations and the contrast induction was studies through imaging. Results are presented (Image 86), for the heart as the main accumulation organ.

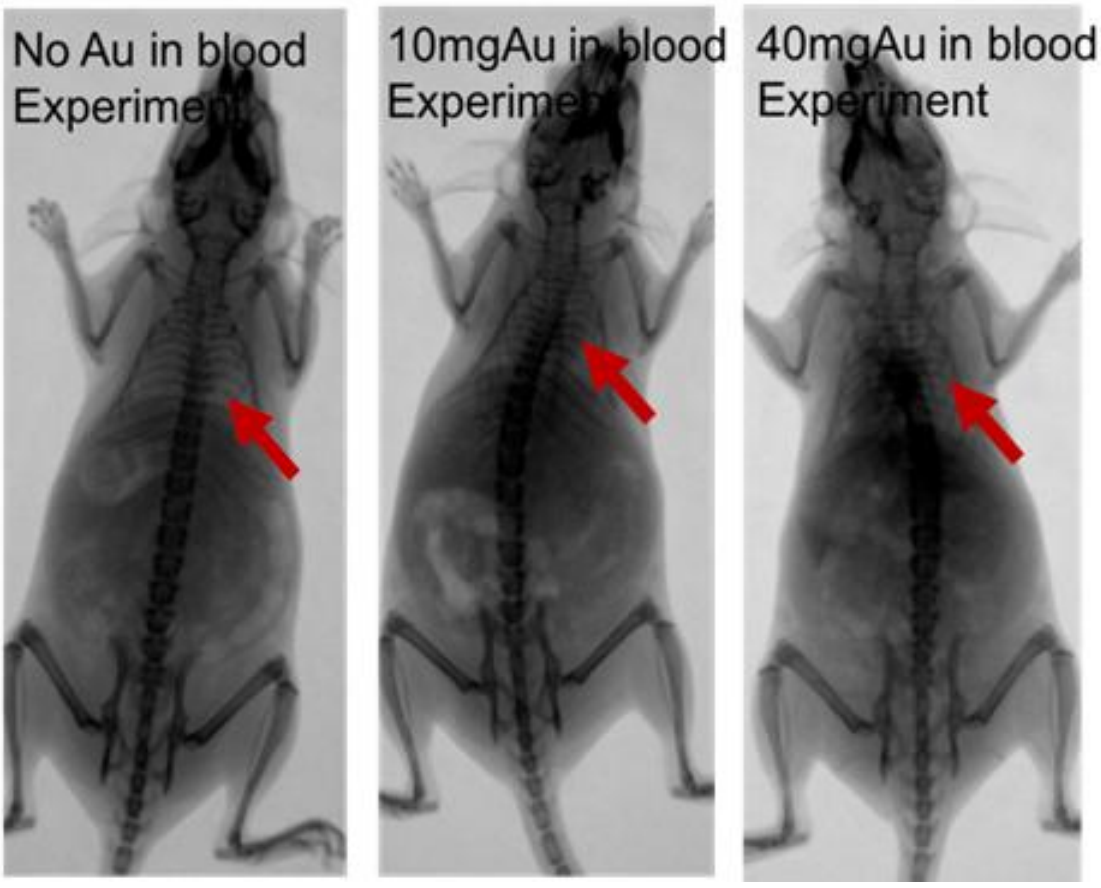

Image 86: X-ray comparison of different levels of Au nanoparticles 15nm(AuroVist) into the bloodstream. Acquisition parameters: 35kVp, 500uAs. The pixel size is equal to 0.1mm

The same compound (AuroVist, Nanoprobes) on its optimal concentration, was again injected in healthy mice and tomographic imaging was performed

on X-CUBE (Molecubes, Belgium) (Image 87)

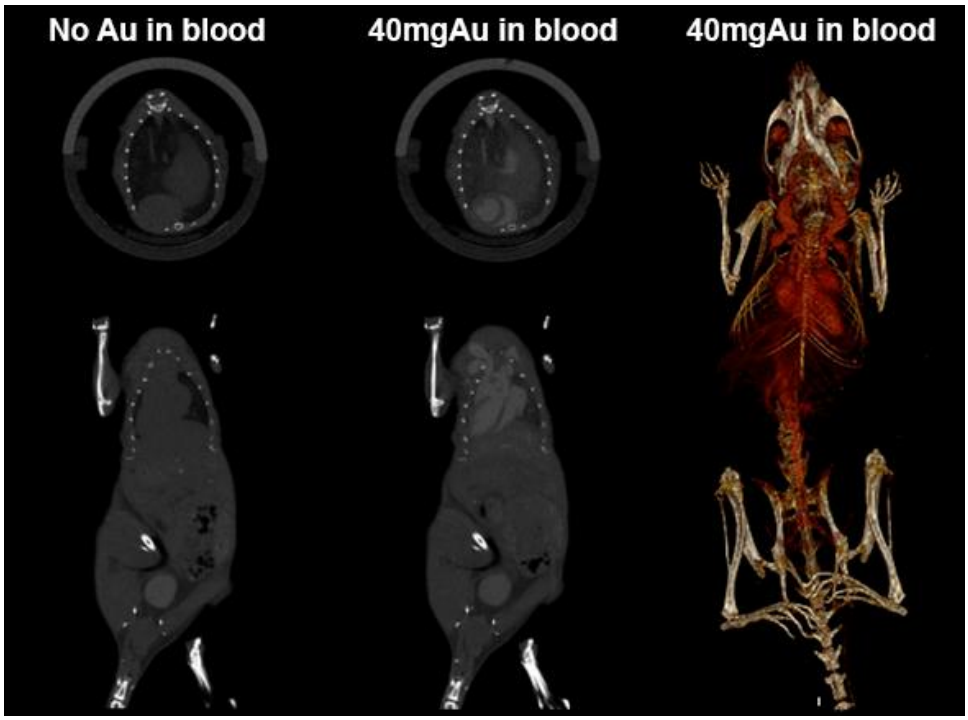

Image 87: CT comparison of coronal and axial slice of different levels of Au nanoparticles 15nm(AuroVist) into the bloodstream followed by a CT rendering (right). Acquisition parameters:40kVp, 350uAs, spiral pitch 1,4mm. Reconstruction paremeters: FDK reconstruction algorithm 100u m voxels size.

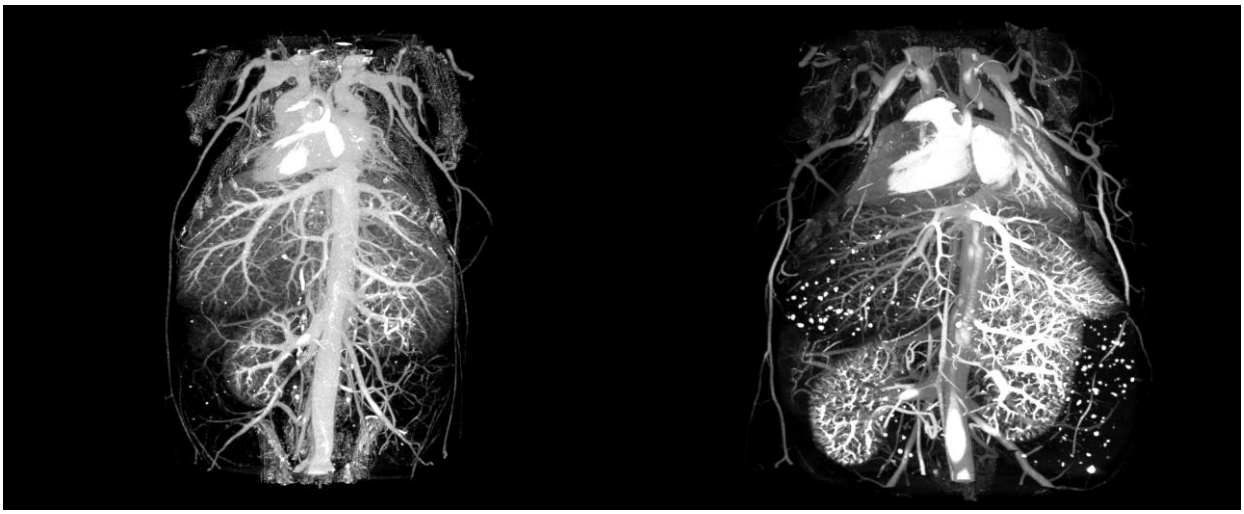

Image 88: 3D rendered CT acquisition. Comparison of control(left) and pathology(right) mouse using contrast agent. Acquisition parameters: 50kVp, 350uAs, spiral pitch 1,4mm. Reconstruction paremeters: ISRA reconstruction algorithm,100um voxels size.

4.5 SPECT experiments

To test the planar SPECT imaging technique (scintigraphy), mice were injected 100 uCi of [99mTc]Tc- MDP – FeCaPs, at a volume of 100 ul with 400μg FeCa per mouse (Image 89). The nuclear imaged were then fused with X-Ray images, as already described, for anatomical co-registration.

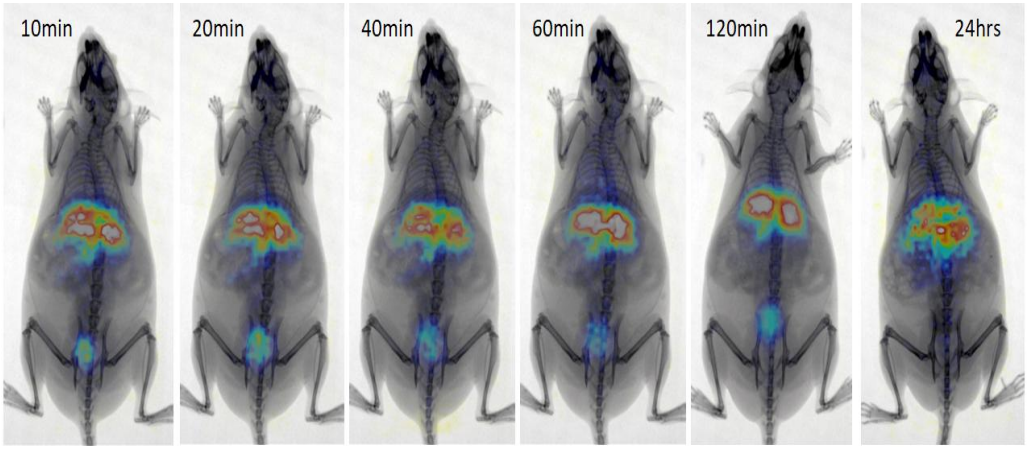

Image 89: Dynamic 2D scintigraphy fusioned with X-ray. 100 uCi of [^{99m}Tc]Tc- MDP – ^{Fe}CaPs 100 ul i.v. injected. 400μg ^{Fe}CaP/mouse.

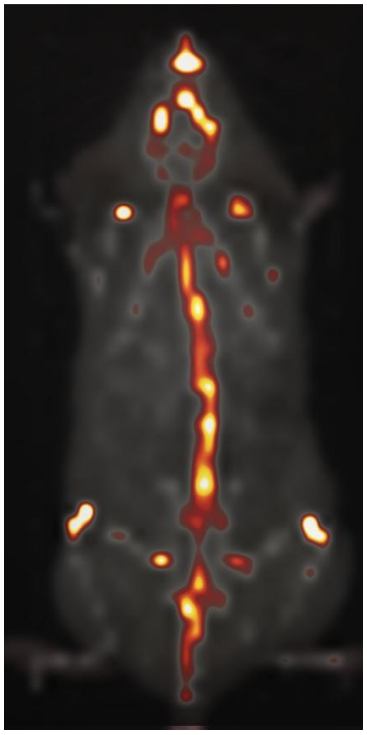

Image 90: Static 2D scintigraphy fusioned with X-ray. 100 uCi of [^{99m}Tc]Tc- MDP –100 ul i.v. injected.

The same mice were then imaged with tomographic SPECT imaging on X-CUBE/γ-CUBE (Molecubles, Belgium) and post processing on VivoQuant (Invicro, Boston). (Image 91)

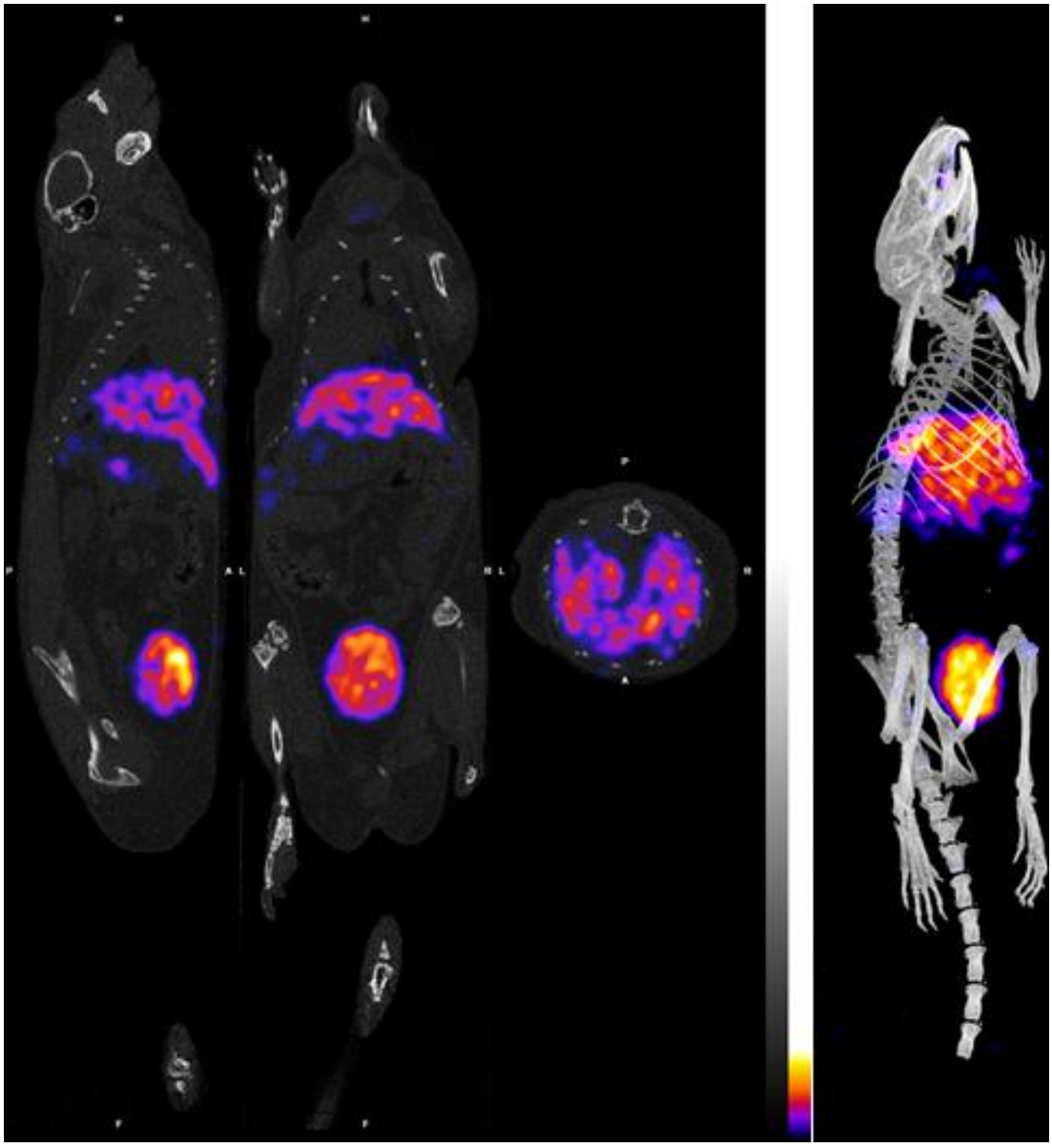

Image 91: SPECT fusioned with CT. [99mTc]Tc-MDP-FeCaPs Concentration: 4-5 mg/mL Injected activity 80 - 100uCi i.v. Acquisition parameters: 30min static using loft hole collimator . Reconstruction Parameters: MLEM reconstruction algorithm 250um voxels size 500 iterations.

4.6 PET experiments

For the planar PET technique (coincidence imaging), oncology mouse models were injected with the clinical tracer 18F-FDG, with an activity of 25 – 35 uCi

and imaged at 1 hour and 2 hours post injection on β-eye^{TM} (BIOEMTECH, Greece). Relevant images can be seen (Image 92), where the tumor sites are highlighted with yellow arrows, as regions of higher accumulation.

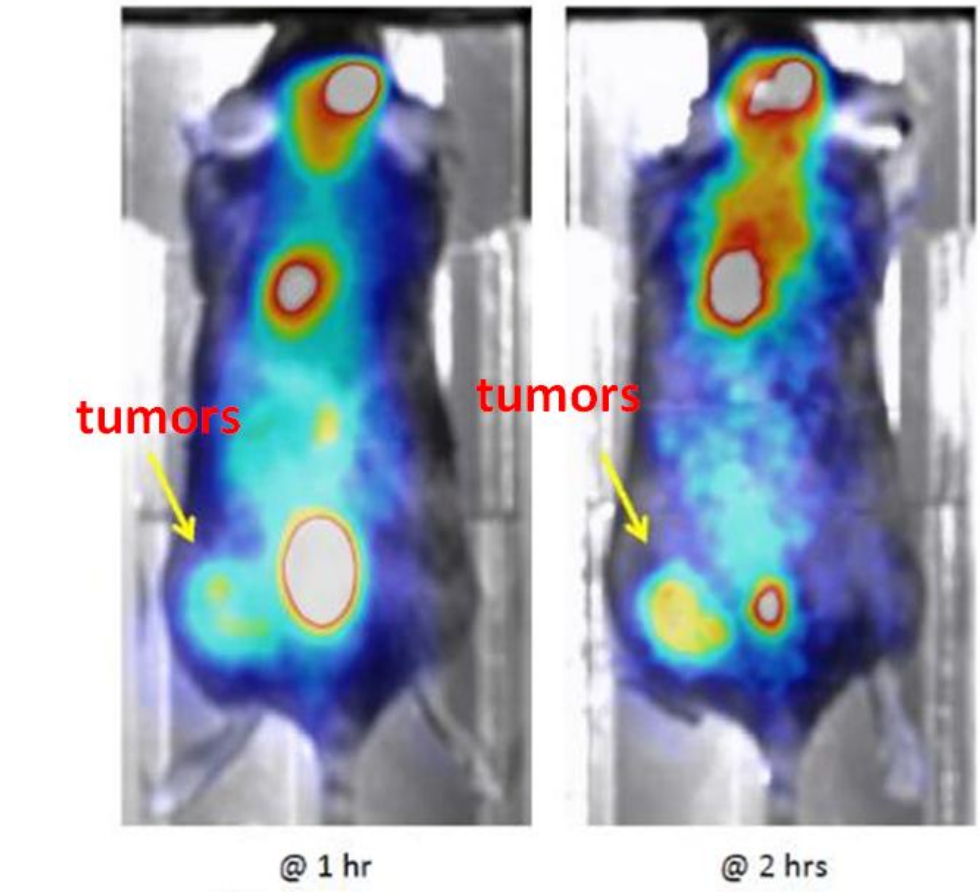

Image 92: PET acquisition fused with optical. Injection through eye vein; 25 – 35 uCi 18F-FDG. Acquisition parameters: 10min static.

this page intentionally left blank

5. Chapter Conclusion

Ionizing radiation imaging systems, due to the intrinsic advantage to penetrate deep into the tissue, provide valuable diagnostic information about the health status of the subject. To summarize, CT is a procedure that is commonly used to image anatomical structures and provides minimal times and high-resolution information. PET and SPECT are mainly used to image the metabolic activity. PET has increased sensitivity if compared to SPECT, because of the absence of a collimator. SPECT can be used to a wide variety of imaging applications, because of the more accurate localization of the signal, in 3D space.

It is worth noticing that preclinical studies are a very important step towards clinical trials and medical implementations, so the evolution in this field is directly related to shorter study time, more robust study results and quicker clinical translation of promising new compounds or drugs.

this page intentionally left blank

6. Publications and Conference Presentations related to this thesis

Publications:

1. Rouchota M, Adamiano A, Iafisco M, Fragogeorgi E, ***Pilatis I,*** Doumont G, Boutry S, Catalucci D, Zacharioudaki A, Kagadis GC. (2021) *'Optimization of in vivo studies by combining planar dynamic and tomographic imaging: workflow evaluation on a superparamagnetic nanoparticles system'*, Molecular Imaging (Accepted for publication, in press).

Conference Presenations:

1. Rouchota M, Fragogeorgi E, Campodoni E, Dermisiadou E, Matzios S, Xanthopoulos S, ***Pilatis I,*** Panopoulos I, Sandri M, Velez M, Bouziotis P & Loudos G. (2019) *'55: Bone Regeneration Assessment Through SPECT/CT Imaging in a Mouse Calvarial Defect Model'*, Transplantation: September 2019 - Volume 103 - Issue 9S2 - p S17 doi: 10.1097/01.tp.0000581368.38449.83
2. Rouchota M, Fragogeorgi E, ***Pilatis I***, Ntari L, Kolokotroni A, Rinotas V, Sarpaki S, Denis MC, Karagianni N, Douni E and Loudos G (2019). *"A preclinical platform for drug evaluation on a RANKL - dependent breast cancer mouse model: in vivo monitoring through PET screening"*, in the 70th National Conference of the Hellenic Society of Biochemistry and Molecular Biology (HSBMB), Eugenides Foundation, Athens Greece, November 29-December 01 2019.
3. Rouchota M, Fragogeorgi E, ***Pilatis I***, Sarpaki S, Adamiano A, Degli Esposti L, Iafisco M, Georgiou M, Bouziotis P, Catalucci D, Loudos G and Kagadis G (2020). *"Optimized imaging protocol for in vivo evaluation of iron-doped nanoparticles using Dynamic Scintigraphy and SPECT/CT"* in the 15th European Molecular Imaging Meeting (virtual EMIM 2020), 24-28 August 2020.
4. Chatzipapas K, Sarpaki S, ***Pilatis I***, Rouchota M, Loudos G and Papadimitroulas P (2020). *"An in-silico study, based on preclinical data,*

for imaging and dosimetry assessment of GNPs in rodents' leg muscle.", in the 15th European Molecular Imaging Meeting (virtual EMIM 2020), 24-28 August 2020.

5. Rouchota M, ***Pilatis I***, Tsialios P, Georgiou M, Fysikopoulos E, Sarpaki S, Loudos G and Kagadis G (2020). "Quantification using 2D scintigraphic versus 3D SPECT imaging in pre-clinical oncology studies: A Comparative Analysis", in the EANM 2020 by the European Association of Nuclear Medicine.
6. Fysikopoulos E, Rouchota M, Eleftheriadis V, Gatsiou C-A, ***Pilatis I***, Sarpaki S, Loudos G, Kostopoulos S and Glotsos D (2021). *"Photograph to X-ray image translation for anatomical mouse mapping in preclinical nuclear molecular imaging",* in MICAD 2021.

7. Training Activities & Certifications related to this thesis

7.1 Training courses

1. "2nd Introduction to Laboratory Animal Technology" organized by the Hellenic Society of Biomedical and Laboratory Animal Science (HSBLAS) at the Laboratory for Research of the Muscoloskeletal System.

2. “52th NCSR Demokritos Summer School”, organized by the European Federation of Organizations for Medical Physics (EFOMP) and the Hellenic Association of Medical Physicists.

3. EuropeanResearchersNight 2018 at Technopolis (Gazi). We had the chance to interact with them and see a fresh insight of our H2020,MSCA MarieCurie research projects (#ERROR #POLYTHEA#VIVOIMAG).

4. EuropeanResearchersNight 2019 at NTUA. We had the chance to interact with them and see a fresh insight of our H2020,MSCA MarieCurie research projects (#ERROR #POLYTHEA#VIVOIMAG)

7.2 Certifications

1. Basic training modules for researchers and personnel who perform procedures (function A), take care of animals (function C), euthanize animals (function D) and design procedures and projects (function B), plus modules 20, 21, 22, 23. Federation of European Laboratory Animal Science Associations, Code Number: F056/16 (FELASA).

this page intentionally left blank

References

[1] C. Suryanarayana and M. G. Norton, "X-Rays and Diffraction," in *X-Ray Diffraction: A Practical Approach*, ed Boston, MA: Springer US, 1998, pp. 3-19.

[2] R. A. Serway, *Physics for scientists & engineers with modern physics*: Second edition. Philadelphia : Saunders College Pub., 1986.

[3] *Diagnostic Radiology Physics*. Vienna: INTERNATIONAL ATOMIC ENERGY AGENCY, 2014.

[4] H. Hu, "Multi-slice helical CT: scan and reconstruction," *Med Phys,* vol. 26, pp. 5-18, 1999.

[5] Γ. Παναγιωτάκης and Ε. Κωσταρίδου, *Βιοϊατρικά Σήματα και Εικόνες: Ιατρική Απεικόνιση με ακτίνες-Χ*. Πάτρα: Πανεπιστήμιο Πατρών, 2014.

[6] C. Doshi, G. van Riessen, E. Balaur, M. D. de Jonge, and A. G. Peele, "Characterization of an indirect X-ray imaging detector by simulation and experiment," *Ultramicroscopy,* vol. 148, pp. 20-24, 2015/01/01/ 2015.

[7] J. H. Siewerdsen, L. E. Antonuk, Y. el-Mohri, J. Yorkston, W. Huang, J. M. Boudry*, et al.*, "Empirical and theoretical investigation of the noise performance of indirect detection, active matrix flat-panel imagers (AMFPIs) for diagnostic radiology," *Med Phys,* vol. 24, pp. 71-89, 1997.

[8] M. Z. Kabir and S. Kasap, "Photoconductors for X-Ray Image Detectors," in *Springer Handbook of Electronic and Photonic Materials*, S. Kasap and P. Capper, Eds., ed Cham: Springer International Publishing, 2017, pp. 1-1.

[9] A. Q. Baron, S. Kishimoto, J. Morse, and J. M. Rigal, "Silicon avalanche photodiodes for direct detection of X-rays," *J Synchrotron Radiat,* vol. 13, pp. 131-42, Mar 2006.

[10] M. Overdick, C. Baumer, K. J. Engel, J. Fink, C. Herrmann, H. Kruger*, et al.*, "Status of Direct Conversion Detectors for Medical Imaging With X-Rays," *IEEE Transactions on Nuclear Science,* vol. 56, pp. 1800-1809, 2009.

[11] M. J. Yaffe and J. A. Rowlands, "X-ray detectors for digital radiography," *Physics in Medicine and Biology,* vol. 42, pp. 1-39, 1997.

[12] T.-T. Kuo, C.-M. Wu, H.-H. Lu, I. Chan, K. Wang, and K.-C. Leou, "Flexible x-ray imaging detector based on direct conversion in amorphous selenium," *Journal of Vacuum Science & Technology A,* vol. 32, p. 041507, 2014.

[13] S. C. Bushong, *Radiologic science for technologists : physics, biology, and protection*: Fifth edition. St. Louis : Mosby, [1993] ©1993, 1993.

[14] D. F. Jackson and D. J. Hawkes, "X-ray attenuation coefficients of elements and mixtures," *Physics Reports,* vol. 70, pp. 169-233, 1981/04/01/ 1981.

[15] L. Gerward, N. Guilbert, K. Bjørn Jensen, and H. Levring, "X-ray absorption in matter. Reengineering XCOM," *Radiation Physics and Chemistry,* vol. 60, pp. 23-24, 2001/01/01/ 2001.

[16] A. I. Hassan, M. Skalej, H. Schlattl, and C. Hoeschen, "Determination and verification of the x-ray spectrum of a CT scanner," *Journal of medical imaging (Bellingham, Wash.),* vol. 5, pp. 013506-013506, 2018.

[17] "The risks of radiation exposure related to diagnostic imaging and how to minimise them," *BMJ,* vol. 342, p. d1920, 2011.

[18] C. H. McCollough and F. E. Zink, "Performance evaluation of a multi-slice CT system," *Medical Physics,* vol. 26, pp. 2223-2230, 1999.

[19] W. A. Kalender, *Computed Tomography: Fundamentals, System Technology, Image Quality, Applications*: Wiley, 2011.

[20] H. Hu, "Multi-slice helical CT: Scan and reconstruction," *Medical Physics,* vol. 26, pp. 5-18, 1999.

[21] A. Christe, J. Heverhagen, C. Ozdoba, C. Weisstanner, S. Ulzheimer, and L. Ebner, "CT dose and image quality in the last three scanner generations," *World journal of radiology,* vol. 5, pp. 421-429, 2013.

[22] T. Flohr, "CT Systems," *Current Radiology Reports,* vol. 1, pp. 52-63, 2013/03/01 2013.

[23] F. R. Verdun, A. Denys, J.-F. Valley, P. Schnyder, and R. A. Meuli, "Detection of Low-Contrast Objects: Experimental Comparison of Single– and Multi–Detector Row CT with a Phantom," *Radiology,* vol. 223, pp. 426-431, 2002.

[24] M. Mahesh, "Search for isotropic resolution in CT from conventional through multiple-row detector," *Radiographics,* vol. 22, pp. 949-62, 2002.

[25] D. D. Cody and M. Mahesh, "Technologic Advances in Multidetector CT with a Focus on Cardiac Imaging," *RadioGraphics,* vol. 27, pp. 1829-1837, 2007.

[26] J. Beutel, H. L. Kundel, and R. L. Van Metter, *Handbook of Medical Imaging: Physics and psychophysics*: SPIE Press, 2000.

[27] L. Zhang, M. W. H. Garming, J. P. Hoogenboom, and P. Kruit, "Beam displacement and blur caused by fast electron beam deflection," *Ultramicroscopy,* vol. 211, p. 112925, 2020.

[28] J. Czechowski, J. Janeczek, G. Kelly, and J. Johansen, "Radiation dose to the lens in sequential and spiral CT of the facial bones and sinuses," *European Radiology,* vol. 11, pp. 711-713, 2001/03/01 2001.

[29] K. C. Tam, S. Samarasekera, and F. Sauer, "Exact cone beam CT with a spiral scan," *Physics in Medicine and Biology,* vol. 43, pp. 1015-1024, 1998.

[30] K. Ichikawa, T. Hara, A. Urikura, T. Takata, and K. Ohashi, "Assessment of temporal resolution of multi-detector row computed

tomography in helical acquisition mode using the impulse method," *Physica Medica,* vol. 31, pp. 374-381, 2015/06/01/ 2015.

[31] W. Huda, A. Sterzik, and S. Tipnis, "X-ray beam filtration, dosimetry phantom size and CT patient dose conversion factors," *Physics in Medicine and Biology,* vol. 55, pp. 551-561, 2009/12/21 2009.

[32] L. Ritschl, F. Bergner, C. Fleischmann, and M. Kachelrieß, "Improved total variation-based CT image reconstruction applied to clinical data," *Physics in Medicine and Biology,* vol. 56, pp. 1545-1561, 2011.

[33] T. G. Flohr, S. Schaller, K. Stierstorfer, H. Bruder, B. M. Ohnesorge, and U. J. Schoepf, "Multi-detector row CT systems and image-reconstruction techniques," *Radiology,* vol. 235, pp. 756-73, Jun 2005.

[34] M. Goitein, M. Abrams, D. Rowell, H. Pollari, and J. Wiles, "Multi-dimensional treatment planning: II. Beam's eye-view, back projection, and projection through CT sections," *International Journal of Radiation Oncology*Biology*Physics,* vol. 9, pp. 789-797, 1983/06/01/ 1983.

[35] A. Holobar and D. Zazula, "Multichannel Blind Source Separation Using Convolution Kernel Compensation," *IEEE Transactions on Signal Processing,* vol. 55, pp. 4487-4496, 2007.

[36] A. Katsevich, "Theoretically Exact Filtered Backprojection-Type Inversion Algorithm for Spiral CT," *SIAM Journal on Applied Mathematics,* vol. 62, pp. 2012-2026, 2002.

[37] L.-C. Man, J. M. Pauly, and A. Macovski, "Multifrequency interpolation for fast off-resonance correction," *Magnetic Resonance in Medicine,* vol. 37, pp. 785-792, 1997.

[38] T. P. Thinh and J. Leroux, "New basic empirical expression for computing tables of X-ray mass attenuation coefficients," *X-Ray Spectrometry,* vol. 8, pp. 85-91, 1979.

[39] R. A. Brooks, "A quantitative theory of the Hounsfield unit and its application to dual energy scanning," *Journal of computer assisted tomography,* vol. 1, pp. 487-493, 1977/10// 1977.

[40] L. W. Goldman, "Principles of CT: radiation dose and image quality," *J Nucl Med Technol,* vol. 35, pp. 213-25; quiz 226-8, Dec 2007.

[41] N. M. Kroll and W. Wada, "Internal Pair Production Associated with the Emission of High-Energy Gamma Rays," *Physical Review,* vol. 98, pp. 1355-1359, 1955.

[42] W. Y. Chang, M. Goldhaber, and R. Sagane, "Radioactivity Produced by Gamma Rays and Neutrons of High Energy," *Nature,* vol. 139, pp. 962-963, 1937/06/01 1937.

[43] M. Donya, M. Radford, A. ElGuindy, D. Firmin, and M. H. Yacoub, "Radiation in medicine: Origins, risks and aspirations," *Global cardiology science & practice,* vol. 2014, pp. 437-448, 2014.

[44] T. E. Peterson and L. R. Furenlid, "SPECT detectors: the Anger Camera and beyond," *Physics in medicine and biology,* vol. 56, pp. R145-R182, 2011.

[45] H. Hemmati, A. Kamali-Asl, and R. Haghshenas, "The Effects of Light Guide Thickness on the Accuracy of Position Estimation, Linearity, and Uniformity Responses of Anger Camera: a Monte Carlo Study," 2015.

[46] R. Foord, R. Jones, C. J. Oliver, and E. R. Pike, "The Use of Photomultiplier Tubes for Photon Counting," *Applied Optics,* vol. 8, pp. 1975-1989, 1969/10/01 1969.

[47] M. Abdelhalim, R. Rizk, H. Farag, and S. Reda, "Effect of energy window width on planer and SPECT image uniformity," *Journal of King Saud University - Science,* vol. 21, pp. 145-150, 07/01 2009.

[48] C. Mestais, N. Baffert, J. P. Bonnefoy, A. Chapuis, A. Koenig, O. Monnet*, et al.*, "A new design for a high resolution, high efficiency CZT gamma camera detector," *Nuclear Instruments and Methods in Physics Research Section A: Accelerators, Spectrometers, Detectors and Associated Equipment,* vol. 458, pp. 62-67, 2001.

[49] F. J. Beekman and G. A. d. Vree, "Photon-counting versus an integrating CCD-based gamma camera: important consequences for spatial resolution," *Physics in Medicine and Biology,* vol. 50, pp. N109-N119, 2005/05/25 2005.

[50] K. Cranley, R. Millar, and T. K. Bell, "Correction for deadtime losses in a gamma camera/data analysis system," *European Journal of Nuclear Medicine,* vol. 5, pp. 377-382, 1980/08/01 1980.

[51] D. Dickerscheid, J. Lavalaye, L. Romijn, and J. Habraken, "Contrast-noise-ratio (CNR) analysis and optimisation of breast-specific gamma imaging (BSGI) acquisition protocols," *EJNMMI research,* vol. 3, pp. 21-21, 2013.

[52] T. Ma, X. Deng, R. Lecomte, and R. Yao, "Derivation of the system matrix for an animal SPECT scanner with rotational collimator and stationary ring detector," in *IEEE Nuclear Science Symposuim & Medical Imaging Conference*, 2010, pp. 2288-2291.

[53] K. L. Greer, C. C. Harris, R. J. Jaszczak, R. E. Coleman, L. W. Hedlund, C. E. Floyd*, et al.*, "Transmission Computed Tomography Data Acquisition with a SPECT System," *Journal of Nuclear Medicine Technology,* vol. 15, pp. 53-56, June 1, 1987 1987.

[54] G. B. Grossman, E. V. Garcia, T. M. Bateman, G. V. Heller, L. L. Johnson, R. D. Folks*, et al.*, "Quantitative Tc-99m sestamibi attenuation-corrected SPECT: Development and multicenter trial validation of myocardial perfusion stress gender-independent normal database in an obese population," *Journal of Nuclear Cardiology,* vol. 11, pp. 263-272, 2004/05/01 2004.

[55] R. Leahy and C. Byrne, "Recent developments in iterative image reconstruction for PET and SPECT," *IEEE Trans Med Imaging,* vol. 19, pp. 257-60, 2000.

[56] J. A. Patton and T. G. Turkington, "SPECT/CT Physical Principles and Attenuation Correction," *Journal of Nuclear Medicine Technology,* vol. 36, pp. 1-10, 2008.

[57] K. A. Wood, P. J. Hoskin, and M. I. Saunders, "Positron emission tomography in oncology: a review," *Clin Oncol (R Coll Radiol),* vol. 19, pp. 237-55, 2007.

[58] F. H. Fahey, "Data Acquisition in PET Imaging," *Journal of Nuclear Medicine Technology,* vol. 30, pp. 39-49, June 1, 2002 2002.

[59] V. Kapoor, B. M. McCook, and F. S. Torok, "An Introduction to PET-CT Imaging," *RadioGraphics,* vol. 24, pp. 523-543, 2004.

[60] L. E. Adam, J. S. Karp, and R. Freifelder, "Energy-based scatter correction for 3-D PET scanners using NaI(T1) detectors," *IEEE Trans Med Imaging,* vol. 19, pp. 513-21, May 2000.

[61] A. Salomon, A. Goedicke, B. Schweizer, T. Aach, and V. Schulz, "Simultaneous Reconstruction of Activity and Attenuation for PET/MR," *IEEE Transactions on Medical Imaging,* vol. 30, pp. 804-813, 2011.

[62] G. K. Kiriiri, P. M. Njogu, and A. N. Mwangi, "Exploring different approaches to improve the success of drug discovery and development projects: a review," *Future Journal of Pharmaceutical Sciences,* vol. 6, p. 27, 2020/06/23 2020.

[63] JoVE Science Education Database, "Model Organisms II: Mouse, Zebrafish, and Chick. An Introduction to the Laboratory Mouse: Mus musculus.," *Journal of Visualized Experiments, Cambridge, MA,* 2014.